Investigation of the Aerodynamic Performance of a DG808s UAS in Propeller Slipstream using Computational Fluid Dynamics

By

Yatish Chandra

Submitted to the graduate degree program in Aerospace Engineering and the Graduate Faculty of the University of Kansas in partial fulfillment of the requirements for the degree of Master of Science.

Chair: Dr. Ray Taghavi

Dr. Shawn Keshmiri

Dr. Saeed Farokhi

Date Defended: August 17, 2017

The thesis committee for Yatish Chandra certifies that this is the approved version of the following thesis:

Investigation of the Aerodynamic Performance of a DG-808S UAS in Propeller Slipstream using Computational Fluid Dynamics

Chair: Dr. Ray Taghavi

Dr. Shawn Keshmiri

Dr. Saeed Farokhi

Date Approved: August 17, 2017

Abstract

Unmanned Aerial Systems (UASs) are relatively affordable and immediately available compared to commercial aircraft. Hence, their aerodynamics and design accuracies are often based on extrapolating from design standards and procedures widely used in the aerospace industry for commercial aircraft with most often, acceptable results. Engineering level software such as Advanced Aircraft Analysis (AAA) use general aviation aircraft data and later extrapolate them onto UASs for aerodynamic and flight dynamics modeling but are limited by their platform repository and relatively high Reynolds number evaluations. UASs however, are aircraft which fly at comparatively low speeds and low Reynolds number with close proximities between the components wherein such standards may not hold good. This thesis focuses on evaluating the accuracy and impact of such industry standards on the aerodynamics and flight dynamics of UASs. A DG808s UAS is chosen for the study which was previously modeled using the AAA software at The University of Kansas by the Flight Systems Team. Using the STAR-CCM+ code, performance data were compared and assessed with AAA. Aerodynamic simulations were carried out for two different configurations viz., aircraft with and without propeller slipstream effects. Data obtained for the non-powered simulations were found to be in good agreement with the AAA model. For the powered flight however, discrepancies between the AAA model and CFD data were observed with large values for the vertical tail side-force coefficient. A comparison with the system identification data from the flight tests was made to confirm and validate this vertical tail behavior with the help of rudder deflection inputs. A relationship between the propeller RPM and the aerodynamic model was established by simulating two different propeller speeds. Based on the STAR-CCM+ data and the resulting comparisons with AAA, updates necessary to the UAS aerodynamic and flight dynamics models currently used in the industry were discussed and concluded with a stress on dependency on higher fidelity methods such as Computational Fluid Dynamics.

Acknowledgements

Firstly, I would like to thank my advisor Dr. Ray Taghavi for all the support and advice he provided me with throughout my master's program. Without his trust and support, I would not have successfully got through some of the toughest courses and times during my time here at The University of Kansas.

Most importantly, I would like to extend my deep gratitude and appreciation to Dr. Shawn Keshmiri for his invaluable guidance throughout my thesis work. Without him, this thesis would never have been possible. I thank him for pushing me hard at every meeting and taking time out of his busy schedule to ensure I succeeded in my research work. This has made me understand what I am capable of and thus made me a better, self-confident person.

I would like to make a special mention to Dr. Saeed Farokhi for always being helpful irrespective of the time of the day. His valuable inputs in interpreting results helped me make good amount of progress in my thesis work.

A huge sense of appreciation goes out to my parents for believing in me in whatever I do and providing me with the best possible education for all these years. Without their emotional and financial support, the aerospace engineering dream of mine would never turn into reality. I am forever grateful and indebted to them and would like to dedicate this thesis to them.

Last but not the least, I would like to specially thank a few people for their help during my thesis work. Aaron, Daksh, Hady, Bella and everyone else in Dr. Keshmiri's Flight Systems Team for their assistance in acquiring important data for the DG808. My fellow undergraduate and graduate students for their help in fixing issues with the 3D CAD model that I initially had. Nick, Dan and everyone else in the Center for Research Computing department for making sure I got enough computing resources and to all my friends here at the university and elsewhere for their emotional support which helped me get through tough times.

Table of Contents

List of Figures

List of Tables

List of Symbols

Symbol	Description	Units
L/D	Lift to Drag ratio	-
C_L	Lift Coefficient	-
C_D	Drag Coefficient	-
C_Y	Side-force Coefficient	-
C_m	Pitching moment coefficient	-
C_l	Rolling moment coefficient	-
C_n	Yawing moment coefficient	-
S	Planform area	m^2
V	Flight speed	m/s
Re	Reynolds Number	-
M	Mach Number	-
K	Turbulent kinetic energy	m^2/s^2
a	Three dimensional lift curve slope	deg^{-1}
a_o	Two dimensional lift curve slope	deg^{-1}
α	Angle of Attack	degree
β	Sideslip angle	degree
ε	Downwash angle	degree
ε_o	Airplane zero angle of attack downwash angle	degree
σ	Sidewash angle	degree

σ_o	Airplane zero sideslip angle, sidewash angle	degree
ω	Turbulent dissipation rate	m^2/s^2
η	Efficiency factor	-
$\frac{\partial \varepsilon}{\partial \alpha}$	Numerical gradient of downwash angle with angle of attack	-
$\frac{\partial \sigma}{\partial \beta}$	Numerical gradient of sidewash angle with sideslip angle	-
$\frac{\partial C_L}{\partial \alpha}$	Numerical gradient of lift coefficient with angle of attack	-
$\frac{\partial C_Y}{\partial \beta}$	Numerical gradient of side-force coefficient with sideslip angle	-

Subscript	**Description**
W	Wing
V	Vertical tail
H	Horizontal tail

Acronym	**Abbreviation**
CFD	Computational Fluid Dynamics
CAD	Computer Aided Design
AAA	Advanced Aircraft Analysis
UAS	Unmanned Aerial System
AOA	Angle of Attack
SST	Shear Stress Transport

Poff	Aircraft configuration with no propulsion unit
Pon	Aircraft configuration with full propulsion unit and rotating propeller
RPM	Revolutions Per Minute
NACA	National Advisory Committee for Aeronautics

Chapter 1 . Introduction

The ability of Unmanned Aerial Systems (UASs) to be used for missions that involve dangerous environments, extreme flying conditions, quick turnaround times between consecutive missions with very limited maintenance have made them a major force in the aerospace research industry. Some of the early use of UASs were in the highly confidential work carried out by the military and air force departments of leading countries. With great advancements in technology over the past few years, the end users of such UASs have widened. Universities, research groups and small scale industries either do not have the resources or sufficient funds to carry out studies using full scale aircraft and thus such groups have started looking into the UAS domain for resources. One of the earliest challenges faced by such groups was the high cost of UASs. However, as mentioned earlier, advancements in technology have allowed such existing expensive technologies to be easily accessible through cost cutting measures such as cheaper fabrication methods and materials, higher production rates and scaled replicas of full wing span UASs. One such example of a low-cost UAS used mainly used by universities and small research groups is the DG808s. The original DG808s sailplane was developed by DG Flugzeugbau for the main purpose of competitions and is quite popular among the gliding community. A scaled 4m wingspan replica of the DG808s with an electric propulsion unit mainly intended for hobby flying and research activities is manufactured by FlyFly and currently used by the University of Kansas as presented in Figure 1.

A major advantage of a UAS is its ability to have autonomous control, thus eliminating human errors which could lead to a reduction in the number of crashes, manpower and further reduction in costs. UASs with such capabilities however have been limited until now and hence several studies and attempts have been successfully made to develop better autonomous systems which are capable of automatic landing and takeoff, collision avoidance, automatic guidance and navigation and remote sensing. Some amount of such work has been conducted with the help of the aircraft shown in Figure 1 at The University of Kansas [1] – [2] by the Flight Systems Team. With these systems however, some amount of human control and input is still required to ensure its proper functioning. Thus, the next goal in research and development is to develop completely autonomous systems in a bid to make the aircraft as safe as possible by eliminating human error

and in the process having higher chances of successful missions with increased performance of the systems.

Figure 1: 4m Wingspan version of the DG808s UAS used at The University of Kansas

The effectiveness of such completely autonomous systems however, depend on the accuracy of aerodynamic, stability and control performance parameters which should be given as input to the onboard systems. This performance prediction is the crux of this thesis. Until now, the Flight Systems Team currently using the DG808s has heavily relied on predictions from the AAA software developed by DARcorporation. AAA is a high-fidelity physics based software capable of estimating the entire envelope of aircraft design such as initial design and sizing, aerodynamics, stability and control analysis and other flight physics applicable to most civil, military and transport airplanes. The methodologies involved are based on [3] and [6] whose formulations are derived from the U.S Airforce Digital DATCOM [7] which is a collection of test data, theoretical estimations with formulations and codes based on correlations to determine the stability and control derivatives of desired aircraft. It makes use of component build up techniques on aircraft and then applies interference effects based on theoretical knowledge, standard practices and test data. AAA uses a similar approach. It correlates geometrical data of aircraft in database (large aircraft with large Re) with the geometry of desired aircraft to model aerodynamics and analyze

flight dynamics. With a heavy use of curve fitting and a combination of component build up with theoretical and empirical calculations of geometrical ratios, the correlational data is achieved. The software like any other, has certain limitations. It falls short in predicting accurate data for low Reynolds number aircraft such as UASs not included in the database. The DG808s has a very unconventional location for the propulsion unit as observed in Figure 1. Due to its uncommon nature in aircraft, limited amount of theory can be used to predict its behavior and hence other methods must be relied upon.

The major objective of this thesis is to establish performance data for the DG808s. To achieve this goal, the highly effective method of Computational Fluid Dynamics (CFD) will be put to use by making use of the commercially popular STAR-CCM+ code. As established through literature studies, CFD has come a long way in predicting performance data of aircraft since its inception. A breakthrough in the industry which confirms this is the heavy use of CFD, around 70% involved in designing the state of the art Boeing 787 Dreamliner aircraft [8]. Unlike AAA which uses preset aircraft data, CFD can be used for a wide range of aircraft ranging from the smallest RC planes to full scale commercial aircraft such as the Airbus A380. Some interesting findings were established for the performance of the tail section of the DG808s in the propeller slipstream as documented in the results section of this report. A comparison of the data obtained was then made with real time flight tests carried out by the Flight Systems Team with good agreements, thus proving the reliability and validity of the CFD performance estimations.

Chapter 2 . Literature review

Several computational studies for UASs and propeller slipstreams have been conducted in the past. Various CFD codes have been employed in these studies yielding a wide range of results which forms a good base for comparison/validation studies. However, preexisting computational studies using a CFD code for the DG808s aircraft in use here, is almost nonexistent. As mentioned in the previous chapter, the current study is of great importance due to the location of the propeller on the aircraft which is quite uncommon. However, studies which are of comparable interests have been referenced here to develop an idea of propeller slipstream and aircraft tail interaction.

2.1 Design and aerodynamic analysis of UASs using CFD

Several research studies have been conducted in the past to design and modify UASs for various missions.

Alejandro Garcia Aguilar [9] made use of CFD to design and develop aerodynamic data of a SBXC glider airframe which was later validated with real time flight test data. The CFD model developed used the $k-\ \omega$ SST turbulence model with a $\gamma-\theta$ transition model to capture the laminar separation bubble for the flight speeds between 10 – 24 m/s. ANSYS CFX software was used to carry out the simulations. Several aerodynamic performance parameters such as the lift, drag force and coefficients, L/D ratios, sink rate, etc., were monitored. The data obtained from the CFD calculations were found to be in close agreement with the previous flight test results until speeds of 15m/s. For flight speeds above 15m/s, some discrepancies were found in the comparison curves which was later attributed to the omission of intricate details on the airframe such as control surfaces, push rods and control servos which could induce disturbances in the flow.

Thomas Hansen [10] carried out CFD simulations to accurately predict the aerodynamic performance of a Standard Cirrus glider using Navier Stokes solvers in the STAR-CCM+ code. A digitizing arm was used to get measurements to design the CAD model required for the CFD analysis. Meshes in the range of 28 – 42 million cells were generated for the different cases. Here again, a $\gamma-\ Re_\theta$ transition model was used along with the $k-\ \omega$ SST turbulence model to accurately capture the laminar separation bubble. 2D airfoil results obtained were compared with available data from NACA and 3D analysis results were compared with the flight test data that was available. 90 km/h and 160 km/h were the range of speeds used for the CFD analysis. Data

obtained from the analysis showed that the aerodynamic parameters such as lift and drag coefficients, glide ratios were in close agreement to the flight test data at the lower range of speeds. However, as the flow velocity shifted towards the higher range, some under and over predictions of the performance characteristics were found which were accounted to the drag created by gaps in the actual airframe.

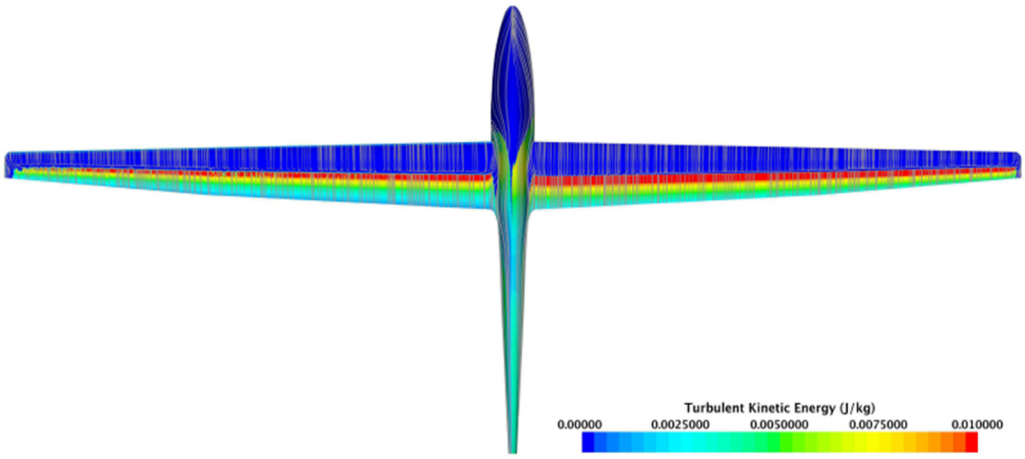

Figure 2: Turbulent Kinetic Energy (J/kg) for a Standard Cirrus glider [10]

Johannes J. Bosman [11], B. Ravi Theja, Dr. M. Satyanarayana Gupta [12] have conducted similar studies on the design and corresponding design refinements and modifications of their respective aircraft using the CFD code: ANSYS FLUENT. Zachary M. Hall [13] used the OVERFLOW CFD code developed by NASA to model the aerodynamic performance of the U.S Military used Shadow 200 airframe, Raven and Gray Eagle UASs.

On summarizing the above mentioned work, it is evident that most of the aircraft used were non powered UASs without the effects of a swirling slipstream from the propeller. In contrast, the DG808s which will be used for the study in this thesis, has a complex configuration where the propeller is mounted right on top of the fuselage with its slipstream directly interacting with the horizontal and vertical tail. Parameters such as downwash in the longitudinal direction and sidewash in the lateral direction will be investigated. In addition to this, the DG808s has a large wing span with a high aspect ratio causing significant changes to the lateral performance of the aircraft vertical tail and will be studied in depth in this thesis.

2.2 Lifting surface in Propeller slipstreams

Several studies on the aerodynamic characteristics of airfoils and wings in propeller slipstreams have been conducted using CFD in the past. Intensive studies for such slipstream-wing interactions have been conducted by Dr. C. Edward Lan [14] in 1974. This study was conducted to confirm the existing theoretical predictions and assumptions on propeller slipstream effects on aerodynamics of lifting surfaces and also to develop a computational method to calculate the performance variations of such surfaces. A modified vortex lattice model made up of two vortex sheets, one for the slipstream region and the other for the region outside it was used to formulate the effects of slipstream. As opposed to other literature that was referenced in this study, variations in the Mach number between the slipstream and the freestream was considered. Computational results obtained were then compared to the experimental data and results from previous studies and were found to be in good agreement with each other. However, the data obtained from the present technique was found to be of much better accuracy with wind tunnel data. The slipstream was seen to split up the wing into two sections viz., downwash and upwash regions as had been presented in previous studies. Variations in lift and drag coefficients along different sections of the wing were found as illustrated by the asymmetric curves. This was attributed to the changes in local angles of attack due to the slipstream components. It was later concluded that in order to accurately predict the variations in aerodynamic coefficients of a wing in slipstream, both radial and axial flow parameters of the slipstream have to be considered along with nonuniformity in Mach numbers between regions in and out of the slipstream. Some of the theories and previous studies used in developing this computational technique are presented in [15]-[17].

One study which is of close relevance to this thesis was conducted by Sparsh A. Chadha, Brent W. Pomeroy and Michael S. Selig [18]. Here, the high-speed wake of a propeller on a 2D airfoil and a 3D wing were studied using ANSYS FLUENT. Initially, a turbulence model comparative analysis was carried out using the $k-\varepsilon$ and the $k-\omega$ SST models. Results of this study indicated that the $k-\omega$ SST turbulence model was more effective and accurate in capturing the turbulent wake of the propeller slipstream and the corresponding aerodynamic coefficients of the airfoil/wing. Symmetric airfoils were placed in the propeller slipstream which was modeled

using an actuator disk in place of the propeller blades at a Reynolds number of 100,000. The geometrical setup is as observed in Figure 3.

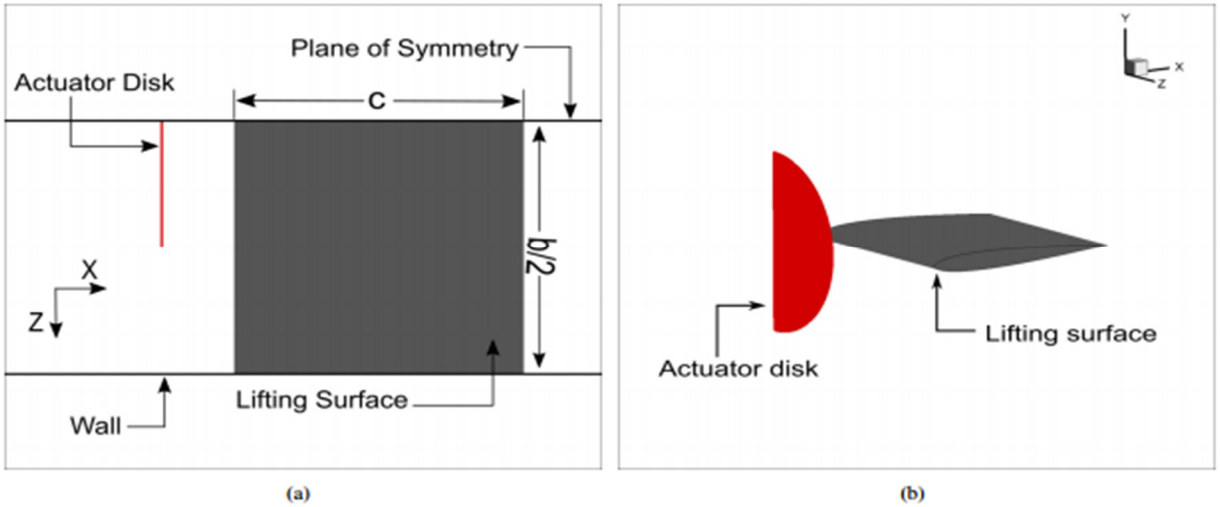

Figure 3: Propeller actuator disk and lifting surface setup (a) Top view (b) Isometric view [18]

Computational results from the two dimensional and three dimensional simulations were compared. For the two-dimensional airfoil analysis, it was observed that the lift and drag coefficients of the airfoil increased in the propeller slipstream as compared to the airfoil in clean air. This was attributed to the fact that the two-dimensional case failed to capture the vortices generated by the propeller rotation in its wake leading to increased aerodynamic performance of the airfoil. Also, the lift curve slope obtained was linear and it failed to capture the stall at high angles of attack. On the contrary, interesting results were seen when the three-dimensional wing was placed in the high-speed propeller wake. On comparison of aerodynamic parameters with the two-dimensional analysis, there were certain regions which showed reduced aerodynamic performance whereas certain regions showed increased performance. A spanwise distribution of the lift on the wing showed that regions of the wing inside the slipstream of the propeller experienced downwash causing a reduction in the local angle of attack thereby leading to reduced aerodynamic coefficients whereas regions outside the slipstream experienced upwash causing increased local angles of attack and hence increased aerodynamic performance in those regions. This was attributed to the presence of counteracting trailing vortices from the actuator disk in the wake.

Weijia Fu, Jie Li and Haojie Wang [19] however conducted similar studies for electric engine propelled gliders with the actual propeller blades rather than approximating it using the actuator disk theory. Simulations were carried out for rotational speeds of 900 – 2000 RPM and a freestream air speed of 13 m/s. Results obtained confirm the findings of [18] that regions of the wing directly in the slipstream experience downwash and vice versa.

The work in [18] however, is based on an actuator disk and close proximity of the lifting surface with the disk. No data is available for an actual propeller and an increased distance between the propeller and the lifting surface which has been accounted for in the current study. It also does not include the effects of different rotational speeds for the propeller which were found to be significant in the performance characteristics of lifting surfaces as presented in the later sections of this report. In [19] even though actual propeller blades were modeled, some aspects were overlooked. The fuselage of the UAS was not modeled thereby neglecting wing-body interactions which impact the lateral directional performance of the vertical tail. In addition to the fuselage, the vertical tail was not included in the study along with the performance characteristics at different angles of attack and sideslip angles. All of these aspects however were looked at in detail in this thesis.

2.3 Propeller Slipstream and Aircraft Tail Interaction

One of the initial studies of propeller slipstream effects on wing and tail of aircraft was carried out by J. Stuper in 1938 [20] which was later published as a NACA report. Wind tunnel flow analysis was conducted for several configurations of the wing and the propeller slipstream to validate theoretical hypothesis laid down by C. Ferrarri [21] and C. Koning. Measurements were made to establish lifting performance of the wing and downwash on the tail in the propeller slipstream. Some interesting and contradicting results were found in comparison to the theoretical assumptions. Firstly, for the wing in the propeller slipstream at small angles of attack, a reduction in the lift was noticed and also flow separation started in regions of the wing outside the slipstream. This reduction in the lift was attributed to the change in the dynamic pressure of the wing in the jet and due to the presence of rotational velocity components in the slipstream which was found to be independent of the angle of attack in linear regions of the lift vs angle of attack curves. Downwash measurements which are an important aspect of the current work, led to another interesting finding wherein the slipstream split the tail section into two regions of counteracting

behavior whose dominance depended on various factors. In one region of the tail, the downwash angle was seen to decrease which contradicted previous findings and theoretical assumptions whereas other regions of the tail had increased downwash angles. The behavior was explained due to opposing sections of tangential velocity magnitudes and to be dependent on factors such as the downwash of the wing alone and orientations of the slipstream w.r.t the tail. It was found that, at some angles of attack, the slipstream completely covered the tail and for other angles of attack the tail was partially covered and in a few cases the slipstream was completely away from the tail leading to varied downwash measurements. Considering all these aspects, it was later concluded that it is hard to make definite assumptions or arguments about the stability contribution of the tail to the whole aircraft in propeller slipstreams.

Based on the computational techniques developed by Dr. C. Edward Lan in [14], a computer program to calculate the lateral directional stability and control derivatives in vortex flows called VORSTAB [22] was developed. The method in subsonic flow was based on Prandtl-Glauert's equations. In this program, the wing was represented using vortex distribution method and later solved using a Quasi-Vortex-Lattice-Method (QVLM). Vortex flow effects such as augmented vortex lift effect, strake vortex and vortex breakdown effects were incorporated. The wing-body interference effect is included by assuming the fuselage flow field effects using Ward's vortex multiplets. The software has certain assumptions in the form of neglecting the wing thickness, boundary layer separation effects and a flat wing wake. However, the program is known to produce respectable results for the stability derivatives in the lateral direction.

Jan Cervinka, Robert Kulhanek and Zdenek Patek [23] conducted studies on an unconventional configuration of the propeller on the aircraft. Initial literature studies carried out indicated a lack of data for aerodynamic performance of aircraft in slipstreams of propellers located at unconventional locations at the rear of the fuselage. To address this issue, a configuration involving the propeller located below the horizontal tail of a T-Tail twin engine scaled aircraft as observed in Figure 4 was put to test in a wind tunnel to establish performance data. The tests were carried out at speeds of 75 and 90 m/s with both clockwise and counter rotating cases for the propeller and finally compared with the more conventional propeller engine aircraft configurations which led to some interesting findings. When both the propellers rotated in the clockwise direction, a large negative yawing moment was produced due to the interaction of the slipstream with the

fuselage and vertical tailplane. However, for counter rotating propellers, contradicting results were found wherein the yawing moment almost reduced to zero. To better understand this complexity,

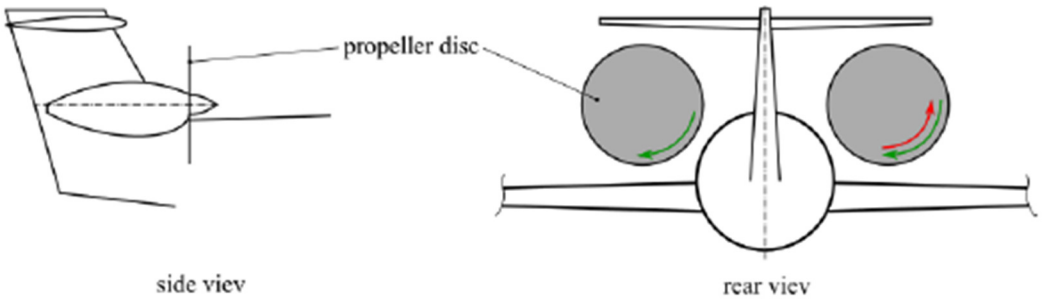

Figure 4: Configuration of aircraft and propellers used for CFD in [23]

smoke flow visualizations on the tailplane were carried out with insignificant results. In addition to the large negative yawing moment created, the propellers seemed to reduce the aerodynamic performance of the horizontal tail. A natural nose up pitching moment of the aircraft was seen to develop due to the higher velocity of the flow underneath the horizontal tail followed by a reduction in lifting characteristics of the horizontal stabilizer due to the reduction of the local angle of attack similar to findings in [18]. Counter rotation of the propellers led to a more profound influence on the horizontal tail characteristics. When the aircraft was placed at different sideslip angles, the yawing moment derivative had high values due to the propeller slipstream which again, increased for counter rotating propellers. This was attributed to the higher side force created due to the inclination of the wind direction (sideslip angle) with the propeller axis. From these findings, it was concluded that the type of rotation of the propellers could not be neglected as was done in previous studies.

M.J.T Schroeijen, L.L.M Veldhius and R. Slingerland [24] carried out an intensive study of the propeller slipstream effect on the vertical tail side wash and corresponding yaw moments on a 1:20 scale model of the Fokker F-27 aircraft with deflected flaps for both engine operative and one engine inoperative conditions. For the sake of simplicity and easy measurements, the horizontal tail was removed from the model at the tail section. Three different types of studies were made viz., measurements in the wind tunnel, potential flow model calculations and a RANS CFD analysis which were in the end compared with one another for validation. Flow conditions across the entire framework was maintained at 40 m/s freestream velocity, a propeller rotation speed of 280 Hz, 0 and 6 degree angles of attack and a flap deflection of 24 degrees. Initial balance

measurements in the wind tunnel showed an increase in the overall yawing moment of the aircraft as a result of a contribution from the vertical tail plane which was later accounted due to the higher sidewash generated in front of the vertical tail due to the rotating propeller slipstream. From this yawing moment calculation, an equivalent sideslip angle was calculated by using Equation (2.1)

$$\frac{\Delta C_n}{\beta} \approx \left(\frac{\partial C_n}{\partial \beta}\right)_T \tag{2.1}$$

where, C_n is the yawing moment coefficient and β is the sideslip angle. This equivalent sideslip angle was found to be on the higher side as compared to a sideslip angle in no slipstream flow. Further study was carried out to determine the cause of this increase in sidewash and it was accounted to the asymmetric distribution of the vortex strength from the wing and the asymmetric shape of the vortex sheet due to roll up. This sidewash further increased with increase in angle of attack due to the asymmetric lift increase of the wing due to increase in angle of attack. These values were then confirmed by placing the aircraft at the above obtained sideslip angles and comparing the proximity of the corresponding yawing moment coefficients. Once these calculations were made using all three methods, a comparative analysis was carried out between them. It was found that the potential flow model largely overestimated and in some cases underestimated the side wash due to its failure to capture the vortex sheet from the wing accurately. In comparison, CFD results were much closer to the wind tunnel measurements and discrepancies in the results were attributed to the numerical diffusion errors present in the CFD simulations due to the relatively coarse grid chosen to limit computational time.

Chapter 3 . Theory

3.1 Propeller Slipstreams

The effects of propeller slipstreams on flow phenomenon has been an important area of study since several decades. Propeller rotation causes a swirling motion of the flow in the wake which when interacts with various structures of the airframe, causes the generation of certain unfavorable forces and moments which create a negative impact on the behavior of the aft lifting surfaces and airplane dynamics in general. One of the most common impacts of propeller slipstream or prop wash is the yawing moment created due to the generation of thrust as explained in [25]. For aircraft with propellers rotating in the clockwise direction, the slipstream interacting with the tail causes the aircraft nose to yaw towards the left i.e., a negative yawing moment and vice versa as observed in Figure 5.

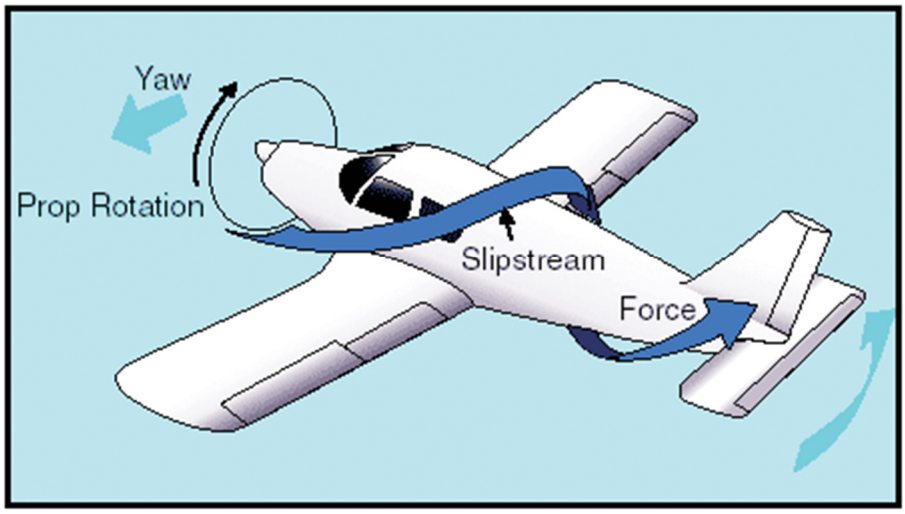

Figure 5: Propeller slipstream behavior on a single engine propeller driven aircraft [25]

This natural yawing motion towards the left is often counteracted by a deflection of the rudder towards the right. Effects of the prop wash on the above yawing motion is exaggerated for aircraft having a single propeller driven engine, low speeds and simultaneous high power settings as is the case with the DG808s UAS. In addition to the yaw imparted to the aircraft by the prop wash, effects can also be seen on the side force generated by the vertical tail, a natural upward pitching moment of the aircraft due to the consequent increase in the downwash on the horizontal tail as seen in [23] and [24] which forces the tail to produce a negative lift at zero angle of attack.

These effects on the horizontal stabilizer are increased when at low speeds, high thrust settings and pusher-propeller type airplanes thereby impacting the overall longitudinal stability of the aircraft. All these flow phenomenon variations due to the propeller slipstream forms the core of this thesis as will be seen in the subsequent sections.

3.2 Downwash

Flow over the forward lifting surface namely the wings creates a trailing vortex system at the tip of the wings called the vortex sheet which is deflected downstream of the wings in both the downward and upward direction thus affecting the characteristics of the aft lifting surfaces viz., the vertical and horizontal tail of the aircraft. This effect of the wing trailing vortex system on the horizontal tail in the longitudinal direction is generally called as downwash as observed in Figure 6. For wings with high aspect ratios and relatively small sweep angles as is the case with the DG808s, the vortex sheet is approximated to be flat even though it is not so.

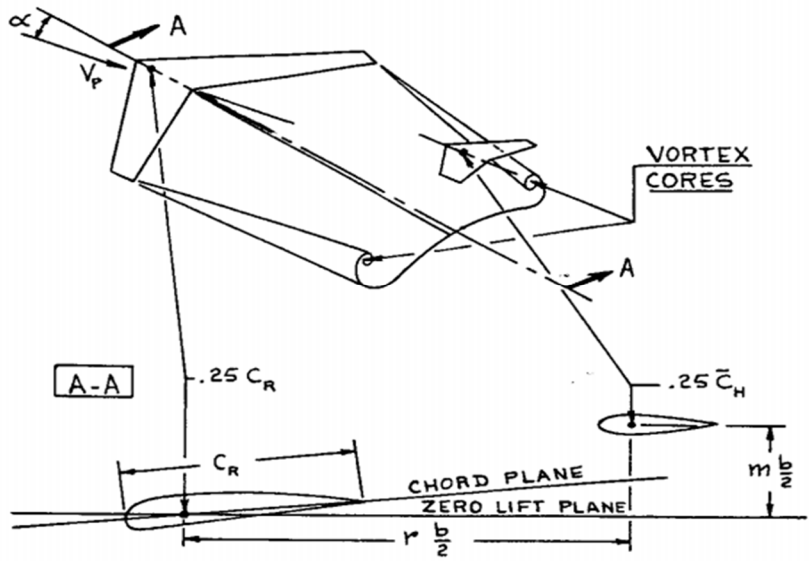

Figure 6: Schematic representation of wing downwash on tail of an aircraft [6]

The calculation of wing downwash is originally based on the Biot Savart's law of 3D vortex distribution from 3D circulation which states that an induced velocity downstream of the wing due to the vortex system is what induces a downwash and is formulated as Equation (3.1) below.

$$\varepsilon = \tan^{-1}\left(\frac{w}{V_\infty}\right) \tag{3.1}$$

where, w is the net downwash along the span of a wing due to the spanwise elliptical lift distribution calculated by integrating for the entire wing span and V_∞ being the freestream velocity. For a wing of finite span, Equation (3.1) can be simplified to Equation (3.2) to calculate the downwash angle.

$$\varepsilon = \pm \tan^{-1}\left[\frac{\pm V_Z \cos\alpha + V_x \sin\alpha}{|V|}\right] \tag{3.2}$$

with, V_x being the axial component of the velocity and V_Z being its perpendicular or upward/downward component of the velocity and α being the angle of attack for the wing.

The downwash effect modeling in general for the horizontal tail of aircraft can be started off using equations in [4]-[6] as mentioned in Equation (3.3).

$$\alpha_H = \alpha_W - \varepsilon \tag{3.3}$$

where, α_H is the effective angle of attack experienced by the horizontal tail due to the downwash ε generated from the wing which is a function of airplane angle of attack α_W.

Now, using Taylor expansion series, a downwash angle estimation can be carried out for airplane zero angle of attack using Equation (3.4) below. The downwash angle ε varies with changes in angle of attack α which is known as the downwash gradient $\frac{d\varepsilon}{d\alpha}$. This downwash gradient forms an integral part of various stability and control derivative calculations.

$$\varepsilon = \varepsilon_0 + \frac{d\varepsilon}{d\alpha}\alpha_W \tag{3.4}$$

For aircraft which fly within the subsonic range, the airplane zero angle of attack downwash angle ε_0 is usually assumed to be negligible and constant which reduces the downwash effectiveness on the horizontal tail to its gradient by substituting into Equation (3.2) as illustrated in Equation (3.5).

$$\alpha_H = \alpha_W - \varepsilon = \alpha_W - \frac{d\varepsilon}{d\alpha}.\alpha_W = \alpha_W\left(1 - \frac{d\varepsilon}{d\alpha}\right) \tag{3.5}$$

To determine the actual effect of the wing downwash on the horizontal tail however, the location of the horizontal tail in relation to the wing both longitudinally and laterally, $r\frac{b}{2}$ and $m\frac{b}{2}$ as observed in Figure 6 plays an important role. In the case of the DG808s which is a T – tail

aircraft where the horizontal stabilizer is placed above and away from the direct wake of the wing, the trailing vortex sheet from the wing has a considerable effect compared to a conventional configuration as explained in [6]. In addition to the proximity of the wing and the horizontal tail, factors such as Mach number (M), aspect ratio (AR), tip ratio (λ) and the sweep angles (Λ) further influence the wing downwash as explained in [4] – [6].

Based on the experimental data and several other mathematical formulations, the equations presented above were formulated along with charts for downwash estimations by the U.S. Air Force in a DATCOM report [7] which was later referenced by [4] – [6]. On the basis of the equations formulated in the DATCOM and the charts provided and using the Prandtl – Glauret transformation, the downwash gradient was then derived as in Equation (3.6) below.

$$\left(\frac{d\varepsilon}{d\alpha}\right)_M = \left(\frac{d\varepsilon}{d\alpha}\right)_{M=0} . \sqrt{1 - M^2} \tag{3.6}$$

where, M is the Mach number and M = 0 denotes the downwash gradient in the incompressible flow regime where the Mach effects are negligible.

Using empirical wing planform relationships and the aid of Polhamus formulae, certain coefficients were formulated based on which the incompressible flow regime downwash angle gradient can be calculated as presented in Equation (3.7).

$$\left(\frac{d\varepsilon}{d\alpha}\right)_{M=0} = 4.44 \left(K_{AR} K_\lambda K_{\mathrm{mr}} \sqrt{\cos(\Lambda_{0.25})}\right)^{1.19} \tag{3.7}$$

where,

$$K_{AR} = \frac{1}{AR} - \frac{1}{1 + (AR)^{1.7}}, \qquad K_\lambda = \frac{10 - 3\lambda}{7}, \qquad K_{\mathrm{mr}} = \frac{1 - \frac{m}{2}}{r^{0.333}}$$

The corresponding charts for these coefficients are present in [4].

Based on commercial aircraft data available, it is assumed that this incompressible regime downwash gradient has negligible variations and hence is taken into consideration as a linear and constant phenomenon.

Significant changes in the downwash angles however can be seen when a propeller slipstream is introduced in the flow as explained in [18]. The variation in downwash now is highly influenced by the relative locations of the propeller slipstream and horizontal tail axes. If the horizontal axis is above the centerline of the slipstream, an increase in the downwash is expected and vice versa. This increase or decrease is attributed to the presence of different components of the downwash introduced by the propeller wake in addition to the component of the downwash due to the existing freestream flow. The resulting downwash angle can now be calculated using Equation (3.8).

$$\varepsilon = (\varepsilon_0)_{PO} + \left(\frac{d\varepsilon}{dC_L}\right)_{PO}\left(C_{L_{PO}} + C_{L_S}\right) + (\Delta\varepsilon)_{\frac{\Delta V}{V_0}=1}\left(\frac{\Delta V}{V_0}\right) \tag{3.8}$$

where, subscript PO indicate the power off configuration where the propeller slipstream is absent, the subscript S indicates the effect of the slipstream, $(\varepsilon_0)_{PO}$ is the zero-lift angle of attack and $\Delta\varepsilon$ is the change in downwash due to inflow.

The downwash phenomenon as explained earlier, is majorly dependent on the proximity of the lifting surfaces (Figure 6). Due to the close distances of the components on UASs as compared to larger commercial airplanes along with significant propeller slipstream effects due to its close proximity to components, the downwash angles could vary by huge margins which can only be estimated through real time simulations. This downwash plays an important role in determining the longitudinal stability and controllability of an aircraft. It is a major factor in the pitching moment calculations presented below in Equation (3.9).

$$C_{m_h} = -C_{L_{\alpha h}}\eta_h\frac{S_h}{S}\left(\bar{X}_{ac_h} - \bar{X}_{cg}\right)\left[\alpha - \left(\varepsilon_0 + \frac{d\varepsilon}{d\alpha}\alpha\right) + i_h + \tau_e\delta_e\right] \tag{3.9}$$

where, C_m is the pitching moment coefficient, $C_{L\alpha}$ is the lift curve slope, S_h/S is the planform area ratio of the horizontal tail w.r.t the wing, $\bar{X}_{ac}$ and $\bar{X}_{cg}$ are the locations of the aerodynamic center and the center of gravity point respectively, i_h is the incidence angle and δ_e is the elevator deflection angle. The subscript h denotes the horizontal tail. The total pitching moment of the aircraft is made up of different components as presented in Equation (3.10). It should always equal to zero or be less than zero for the system to be stable.

$$C_m = C_{m_{ac_{wf}}} + C_{m_{wf}} + C_{m_h} = 0 \tag{3.10}$$

where the subscripts ac_{wf} represent the wing-fuselage contribution and h is the horizontal tail contribution.

In Equation (3.9), all the terms except ε_0 and $\frac{d\varepsilon}{d\alpha}$ are assumed to remain constant in flight. An inaccurate assumption of the downwash variables could lead to huge instabilities of the system/aircraft leading to extremely large control inputs to make the system stable again. This downwash effect estimation is the major motivation behind this thesis.

3.3 Vertical Tail Side-force and Sidewash

For aircraft flying at a sideslip angle β or when the wind makes an angle relative to the C.G point, a force is generated in the lateral direction which affects the lateral and dynamic stability of the aircraft. This force is generally called the side force and is made up of the contribution from different body components of the aircraft such as the wing, fuselage, wing-fuselage interaction, the horizontal tail, nacelle and Pylon. An aircraft with a positive sideslip angle is as illustrated in Figure 7. According to established sign convention, when the relative wind is incoming through the pilot's right ear, the resulting sideslip angle is positive and vice versa. In other words, aircraft yaw towards the left is considered to be a positive sideslip.

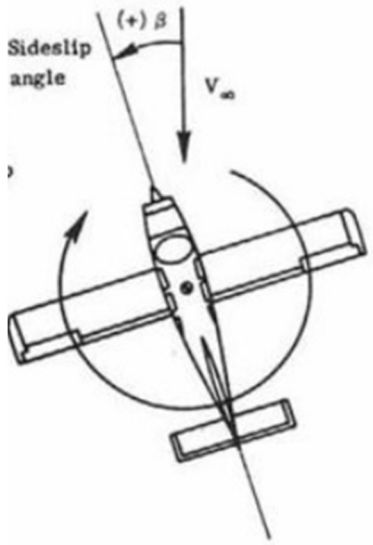

Figure 7: Schematic representation of sideslip angle sign convention [53]

Similar to the downwash angle ε in the longitudinal direction that was explained in section 3.2, a lateral directional counterpart called the sidewash angle σ exists due to the sideslip angle β

of the aircraft. The sidewash angle modeling is similar to the downwash angle modeling presented in section 3.2 and is illustrated in Equation (3.11) below.

$$\sigma = \sigma_0 + \frac{\partial \sigma}{\partial \beta}.\beta \tag{3.11}$$

where, σ_0 is essentially the sidewash angle at zero sideslip angle, similar to ε_0 for the downwash modeling and $\frac{\partial \sigma}{\partial \beta}$ is the sidewash angle sensitivity to the sideslip angle. In [4]-[6], σ_0 is assumed to be negligible which leads to the relation in Equation (3.12).

$$(\beta - \sigma) = \beta - \left(\frac{\partial \sigma}{\partial \beta}\right)\beta = \left(1 - \frac{\partial \sigma}{\partial \beta}\right)\beta \tag{3.12}$$

Sidewash effect in general is considered to be of a much smaller magnitude as compared to the downwash effect. That assumption holds good as long as the sidewash angles and gradients are accurately measured. Inaccurate measurements and assumptions of σ_0 and $\frac{\partial \sigma}{\partial \beta}$ however could have effects larger than the downwash on the stability of the aircraft as explained through Equations (3.13) and (3.14) below.

$$C_{l_{\beta_v}} = -C_{Y_{\alpha_v}}\left(1 - \frac{\partial \sigma}{\partial \beta}\right)\eta_v \frac{S_v Z_{v_s}}{Sb} \tag{3.13}$$

$$C_{n_{\beta_v}} = -C_{Y_{\alpha_v}}\left(1 - \frac{\partial \sigma}{\partial \beta}\right)\eta_v \frac{S_v X_{v_s}}{Sb} \tag{3.14}$$

Subscript v represents the vertical tail, $C_{l_{\beta_v}}$ and $C_{n_{\beta_v}}$ represent the rolling moment coefficient and the yawing moment coefficient of the aircraft respectively, η_v is the vertical tail efficiency factor, $\frac{S_v}{S}$ is the planform ratio of the vertical tail w.r.t the wing, Z_{v_s} and X_{v_s} are the distances along the stability Z and X axes from the vertical tail aerodynamic center to the airplane center of gravity respectively. Similar to Equation (3.9), since all the factors in the above equations are constant, wrong assumptions of sidewash and its gradient can cause the system/aircraft to be highly unstable in the lateral direction.

The lift coefficient of the vertical tail in the lateral direction due to the sideslip angle is called the side force coefficient denoted by C_Y. As per convention, for symmetric aircraft and a linear behavior of the vertical tail, a positive sideslip angle should produce a negative C_Y and a negative sideslip angle should produce a positive C_Y. This linear behavior is expected for symmetric aircraft. As mentioned earlier, the side-force coefficient is made up of several components which are presented in the relation (3.15) below.

$$C_{Y\beta} = C_{Y\beta_{WB}} + C_{Y\beta_H} + C_{Y\beta_V} \tag{3.15}$$

where, $C_{Y\beta}$ is the sensitivity/variation of the side-force due to the sideslip angle β represented by $\frac{\partial C_Y}{\partial \beta}$ and subscripts WB, H and V represent the side-force components of the Wing-Body interaction, Horizontal tail and the Vertical tail respectively.

The side-force contribution of the wing-body interaction is highly dependent on the dihedral angle of the wing and the shape of the fuselage. As explained in [5], the wing does not contribute directly to the side-force, however it affects side forces generated by other components of the aircraft and is presented in Equation (3.16). This wing component of the side force coefficient is confirmed by the current CFD analysis and is illustrated in section 6 of the report.

$$C_{Y_{wing}} = -C_{D_{wing}} \triangleq -C_{D_{parasite-wing}} = k\Gamma^2 \tag{3.16}$$

where, $C_{D_{parasite-wing}}$ is the parasitic drag coefficient of the aircraft, k is an interference factor and Γ is the dihedral angle of the wing. Contribution of the horizontal tail is usually considered to be negligible for T-Tail aircraft as in the case of DG808s, but an end plate effect is often observed as explained in [5].

The most significant contribution to the side force however is due to the vertical tail or in other words the fin effect as mentioned in [5] and forms an important role in this thesis as will be presented in Section 6. Based on empirical relations laid out in the U.S Airforce DATCOM [7], a relationship for the vertical side force is modeled as in Equation (3.17).

$$C_{Y_{\beta V}} = -K_{Y_V}.\left|C_{L_{\alpha v}}\right|\eta_v.\left(1+\frac{\partial \sigma}{\partial \beta}\right)\frac{S_v}{S} \qquad (rad^{-1}) \tag{3.17}$$

where, $C_{L_{\alpha v}}$ is the lift curve slope coefficient of the vertical tail, η_v is the vertical tail efficiency, S_v and S are the planform areas of the vertical tail and the aircraft respectively. K_{Y_V} is an empirical

factor which is based on geometry of the vertical tail and the aircraft. A graph consisting of the values are present in [4].

As explained further in [5], the side-force coefficient of the vertical tail is further influenced by propeller slipstream effects wherein the swirl changes the local sideslip angle β experienced by the vertical fin and also increases the dynamic pressure ratio at the vertical tail. Further, it is mentioned that the side-force coefficient also varies with changes in angle of attack of the airplane α, for moderate to high α wherein a significant side force component may be observed at zero sideslip angle β. A detailed study of this is present in Section 6.

Chapter 4 . DG808s Design Specifications

The DG808s is originally a sailplane developed by DG Flugzeugbau for the use of competitions. The sailplane is a manned version with a wingspan of 15 or 18m. An unmanned aerial version of this aircraft is manufactured by FlyFly with a wingspan of 4m. This scaled UAS version of the DG808 is used for various purposes such as research and hobby flying. Several studies have been conducted at The University of Kansas using the DG808s to develop automatic cross wind landings, wind estimation, traffic collision avoidance system, etc. However, a 3D CAD model of the aircraft was not readily available and had to be developed from scratch by obtaining measurements from the actual airframe. The CAD software, NX 8.5 developed by Siemens was used to model the aircraft.

4.1 Wing

The DG808s UAS, like all gliders makes use of a large aspect ratio wing to have the L/D ratio as large and effective as possible. Wings on this aircraft make use of the HQ 2512 cambered airfoil as shown in Figure 8(a). This airfoil is mainly a low Reynolds number airfoil and is widely used among gliders all over the world due it's capability of producing high lift at low Reynolds numbers and low angles of attack. The ailerons and flaps which form the control surface devices of the wings were not modeled for the sake of simplicity.

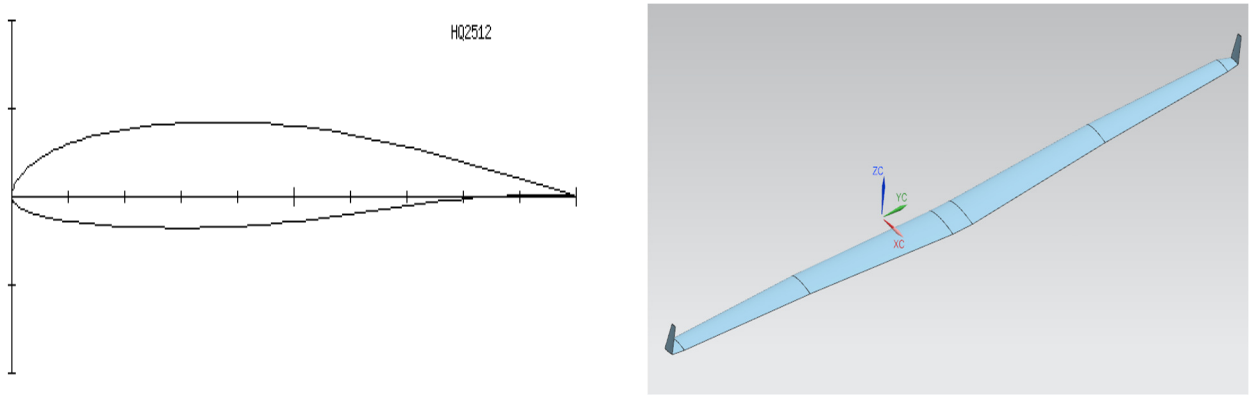

(a) (b)

Figure 8: Schematic representation of the primary lifting surface on the DG808s (a) 2D Airfoil (b) 3D CAD wing model

Some of the main design parameters of the wing in the developed CAD model are listed in Table 1.

Table 1: Design parameters of the DG808s wing

Design parameter	Values (m)
Wing span	4
Root chord length	0.2
Tip chord length	0.06
Wing Taper ratio	0.0762
Leading edge sweep angle	3.5 deg
Trailing edge sweep angle	-1.8 deg
Dihedral Angle	1.5 deg
Wing area	1.908048 m^2
Wing aspect ratio	25.89
Quarter chord sweep angle	2.2 deg

4.2 Fuselage

The fuselage of the DG808s was modeled using 15 different sections along the length. Measurements at each of these sections were picked up from the actual aircraft and then manually input into the CAD software. Since the DG808s has non-retractable landing gears/wheels and the canopy blends into the curvature, they were incorporated into the fuselage to simplify the model for CFD analysis.

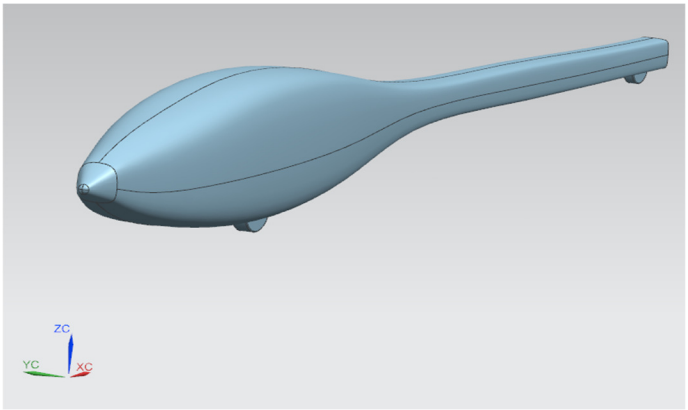

Figure 9: 3D CAD model of theDG808s Fuselage

Resulting dimensions of the fuselage are as listed in Table 2.

Table 2: Design parameters of the DG808s fuselage

Dimensions	Values (m)
Length	1.423416
Planform area	0.405384 m^2
Maximum height	0.039624
Wetted area	1.328928
Maximum width	0.149352
Maximum diameter at wing-fuselage intersection	0.158496

4.3 Horizontal and Vertical tail

The tail section of the aircraft forms an integral part of the study in this thesis and hence its design was carefully evaluated. As in most of the gliders and aircraft, both the horizontal and the vertical tail use symmetric airfoils for their design as they are not considered to be primary lifting surfaces. The horizontal tail makes use of the n0009 (9% smooth) airfoil developed by NACA as shown in Figure 10 (a-b).

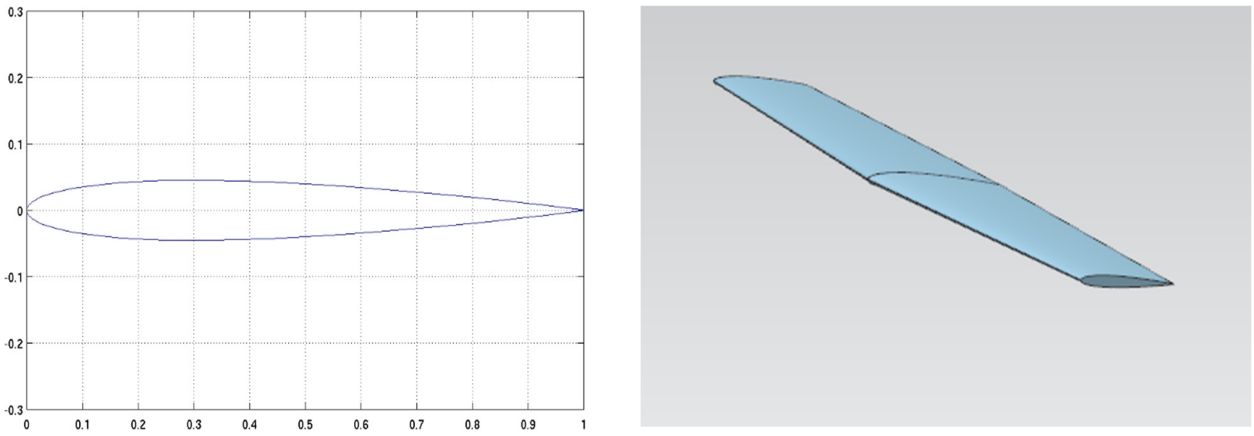

(a) (b)

Figure 10: Schematic representation of the horizontal tail section of the DG808s (a) 2D Airfoil (b) 3D CAD model

The aft control surfaces such as the elevator on the horizontal tail and rudder on the vertical tail were not included in the final CAD model for the sake of simplicity. Corresponding design parameters for the horizontal tail are listed in Table 3.

Table 3: Design parameters for the DG808s horizontal tail

Design parameter	Value (m)
Root chord length	0.170688
Tip Chord length	0.12192
Taper ratio	0.21336
Leading edge sweep angle	7.6 deg
Trailing edge sweep angle	2.5 deg
Area	0.27432 m^2
Aspect ratio	3.91
Quarter chord sweep angle	5.1 deg

A NACA 0012 airfoil is used in designing the vertical tail of the aircraft as observed in Figure 11 (a-b).

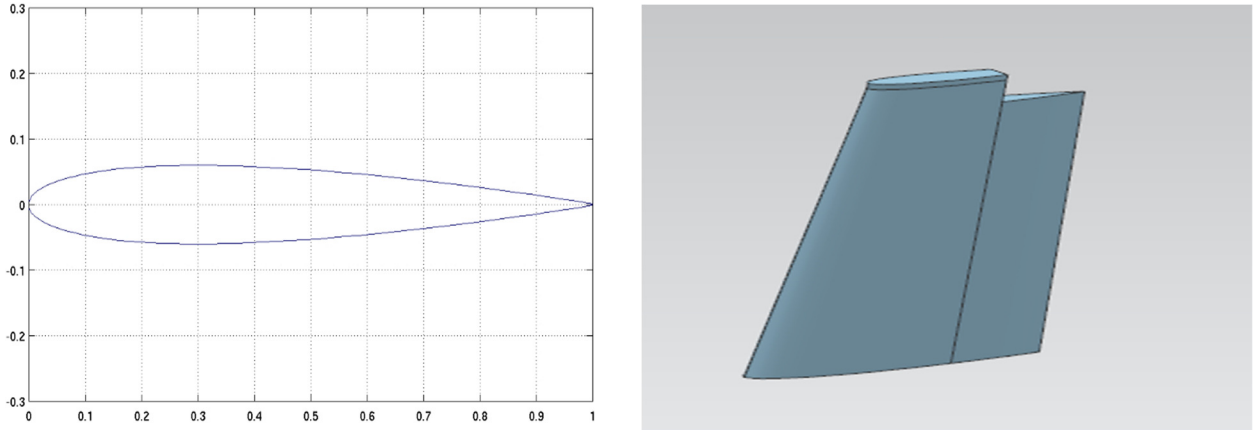

(a) (b)

Figure 11: Schematic representation of the vertical tail section of the DG808s (a) 2D Airfoil (b) 3D CAD model

Design parameters for the vertical tail are listed in Table 4.

Table 4: Design parameters for the DG808s vertical tail

Design parameter	Value (m)
Root chord length	0.2286
Tip Chord length	0.170688
Taper ratio	0.2286
Leading edge sweep angle	10.8 deg
Trailing edge sweep angle	-1.4 deg
Area	0.173736 m^2
Aspect ratio	1.33
Quarter chord sweep angle	7.8

4.4 Propulsion unit

As with the tail section of the aircraft, the propeller and the corresponding parts of the power plant system were carefully designed since they form an important part of the current study. The electric propulsion system on the DG808s UAS is made up of an electric motor, vertical pylon, a nacelle and a two-bladed propeller. All these components are mounted on the fuselage of the aircraft making it a pusher type propulsion unit. Again, since no 2D drawings of the unit were available, measurements were made on the actual parts of the aircraft which were later traced and converted into 3D models on the NX CAD software.

4.4.1 Pylon and Nacelle

The DG808s UAS consists of a vertically mounted pylon made up of two different types of airfoils viz., the NACA 0011 airfoil at the root of the pylon and the nacelle and an e864 airfoil at the root of the pylon and the fuselage. Corresponding dimensions of the pylon are listed in Table 5.

Table 5: Design parameters of the DG808s pylon

	Design parameter	Value (m)
n0011 Airfoil	Root and tip chord	0.06184392
	Span	0.140208
	Dihedral	85 degrees
	Thickness ratio	30
	Wetted area	0.06096 m^2
	Aspect ratio	2.26
e864 Airfoil	Root and tip chord	0.00509016
	Span	0.216408
	Dihedral	90 degrees
	Thickness ratio	30
	Wetted area	0.009144 m^2
	Aspect ratio	42.41

Since the nacelle had no base geometrical data, it was modelled using measurements from the actual part and it was made sure the final model was as close to the original part as possible. The final design parameters are listed in Table 6. Once the nacelle and the pylon were designed, they were united together as a single body as observed in Figure 12.

Table 6: Design parameters of the DG808s nacelle

Design parameter	Value (m)
Base area	0.006096 m^2
Planform area	0.0235 m^2
Length	0.140208
Maximum frontal area	0.009144 m^2
Wetted area	0.073152 m^2

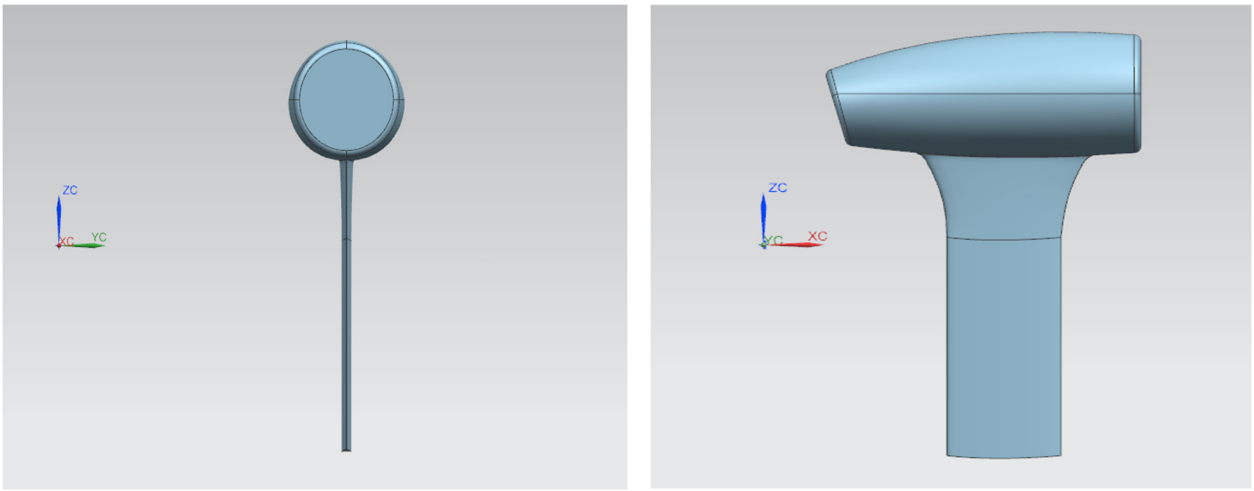

(a) (b)

Figure 12: 3D CAD models for the united pylon and nacelle (a) Front view (b) Side view

4.4.2 Two Bladed Propeller

The propeller fan blades on the DG808s are made up of varying chord length sections of a NACA 0012 airfoil. To be more precise, 9 different sections were used to make up an entire propeller blade as shown in Figure 13.

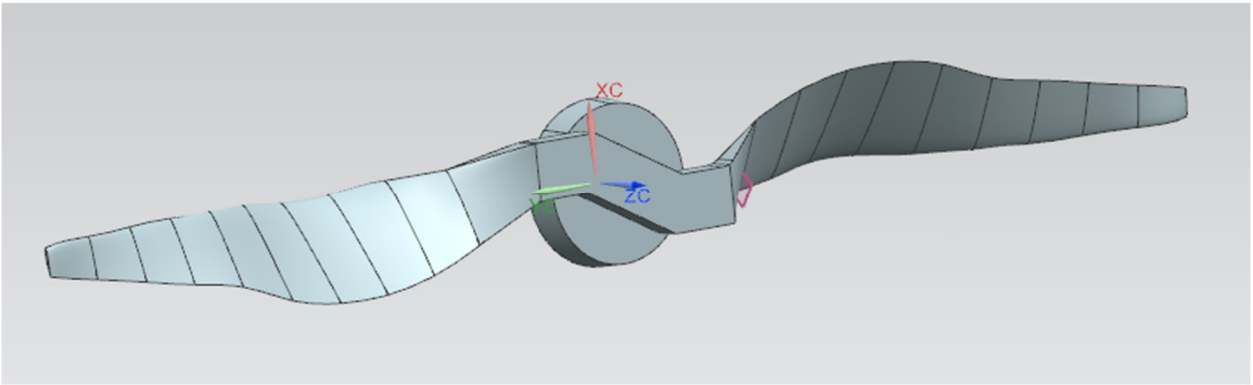

Figure 13: 3D CAD model of the DG808s propeller

The propeller blades were then placed on a rotating cylindrical hub of 0.055m diameter. The corresponding dimensions of the propeller are listed in Table 7. The final model of the propeller was then assembled onto the pylon and nacelle unit and it was made sure that the centerline of the propeller hub and the nacelle overlapped forming the point of rotation for the propeller and thus avoiding wobbling issues. The electric propulsion unit of the

Table 7: Design parameters of the DG808s propeller blades

Design parameter	Value (m)
Root chord length	0.0160799
Tip Chord length	0.0062957
Maximum sectional chord length	0.0208738
Total Propeller diameter	0.3048
Pitch	0.2159
Hub diameter	0.0365125

DG808s uses a 1200 KV brushless motor to generate power and propel the aircraft forward. The maximum rotational speeds for the propeller vary from 5000 to 11,000 RPM on a test bed for different throttle inputs. Sufficient data however is not available for the throttle inputs required to achieve the same amount of RPM and power as that of the test bed data in flight. In the current study however, the RPM is maintained at 6500 RPM which is the ideal cruise RPM rating and 10,000 RPM for cases simulated in the upper limit of the range.

4.5 Final 3D Assembly

Once the separate parts were modelled, an assembly file containing all the parts was then created as presented in Figures 14 – 16. The propulsion unit was mounted on the fuselage such that the centerline of the pylon was in line with the C.G point of the aircraft. This meant that the distance between the face of the hub of the propeller and the leading edge point of the horizontal tail at the root section was 0.8 m with a slight vertical offset in the centerlines of the propeller hub and the chord line of the horizontal tail.

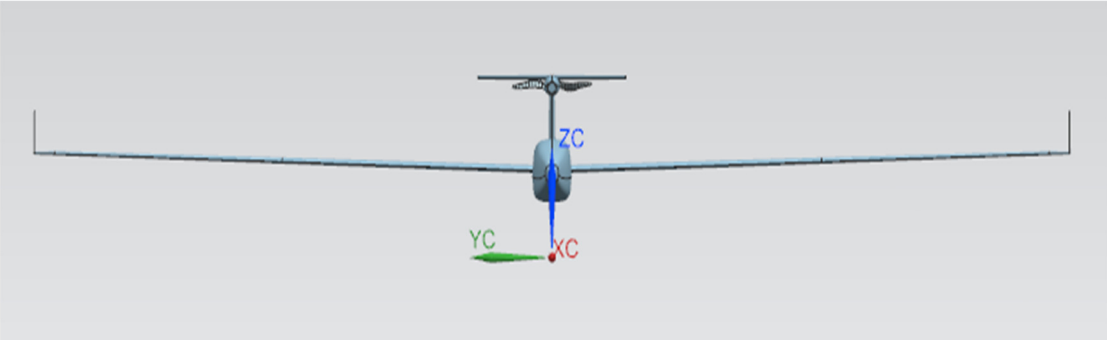

Figure 14: Front view of the DG808s 3D CAD model

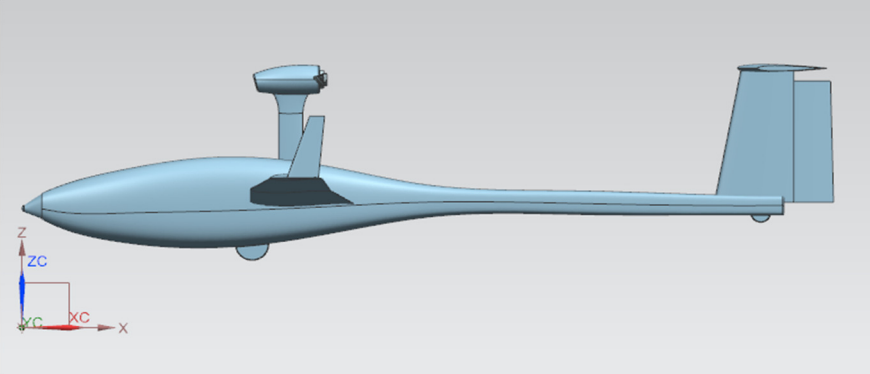

Figure 15: Side view of the DG808s 3D CAD model

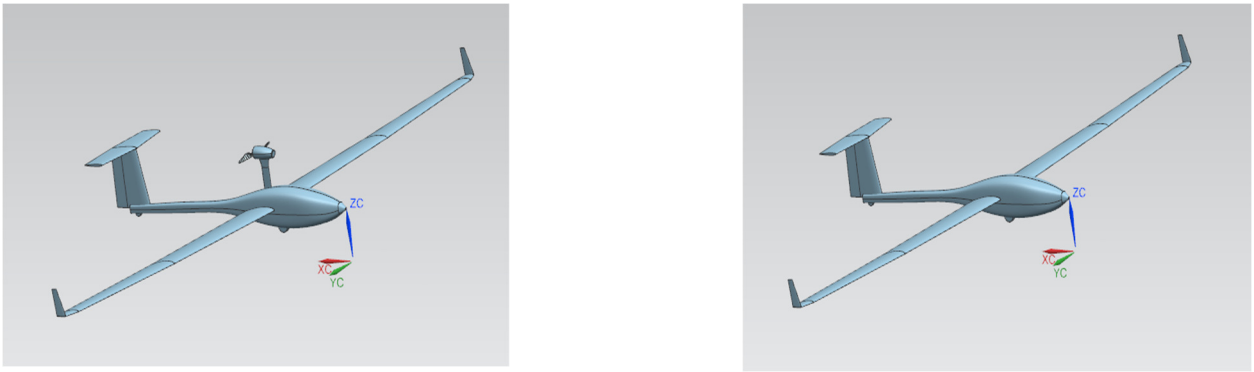

(a) (b)

Figure 16: Different configurations of the DG808s (a) Pon: with the propulsion unit (b) Poff: without the propulsion unit

To model the rotation of the propeller in STAR-CCM+, a cylindrical computational domain as observed in Figure 17 for the propeller was modeled in the CAD package itself before importing it into the CFD code as a parasolid file.

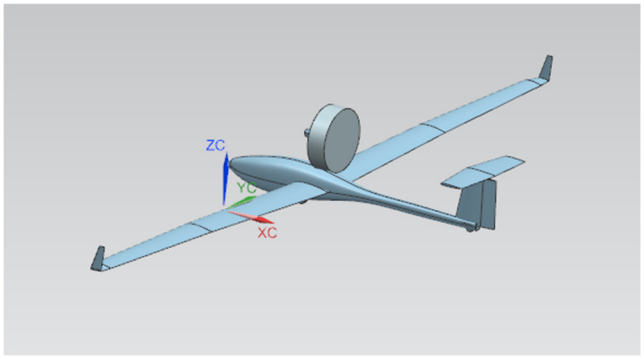

Figure 17: Isometric view of the DG808s 3D CAD model with rotational domain for the propeller

Chapter 5 . CFD Analysis

To study the aerodynamic performance of the DG808s UAS which is the main objective of this thesis, a suitable CFD code had to be first selected. Two widely used commercial CFD softwares viz., ANSYS and STARCCM+ were available in the aerospace engineering department at The University of Kansas. After comparing several aspects such as in-built CAD capabilities, complexity of mesh generation, physics models, computational time and user friendliness, the STARCCM+ code developed by CD-adapco was considered suitable for the current work. The ability to handle complex geometries and make changes to the CAD model within the code with relatively low computational runtimes has made STARCCM+ very popular in the commercial aerospace industry.

5.1 Continua and Physics Models

Before the start of any CFD analysis, it is necessary to first understand the flow physics involved in the problem to accurately predict the flow characteristics. For the study in this thesis, physics models suitable for three dimensional, low Reynolds number and rotating flows were studied.

As a result of the low speeds at which the DG808s flies, the effects due to compressibility were neglected leading to the choice of a constant density gas coupled with the segregated flow solver. Considering the very low altitudes of flight, the air density was kept at sea level value of 1.223 kg/m^3. The average Reynolds number based on the mean aerodynamic chord of the wing was around 2x10^5.

Considering various aspects such as computational time, cost and other constraints, the simulations were maintained as steady state which solves the momentum equations for a single instance of time. In reality however, all flow phenomenon including the flow around an aircraft is unsteady i.e. varies with time, however it is possible to impose a steady condition to establish baseline performance data. One of the challenges in CFD is the selection of an ideal turbulence model for the problem in hand. However, from the literature data and previous research, it has been proven that the Spalart Allmaras (SA) and the $k-\omega$ turbulence models are best suited for external aerodynamic analyses which is the case in this thesis. The Spalart Allmaras (SA)

turbulence model is effectively a low Reynolds number one equation model designed for the study of aerodynamic flows especially in the aerospace industry. The model is based on solving a transport equation for the turbulent viscosity $\bar{\nu}$ and is computationally less expensive since only one equation is being solved. However, the model fails to accurately predict flows with separation such as high angles of attack on airfoils and wings making it unsuitable in the current application. In such cases, the $k-\omega$ model has proven to be the most accurate.

5.1.1 $k-\omega$ turbulence model

The $k-\omega$ SST (Menter's Shear Stress Transport) model was initially developed by F.R Menter in 1994 especially for applications in the aerospace industry. It solves two equations viz., turbulent Kinetic energy 'k' and the eddy dissipation rate 'ω' which are as follows:

$$\frac{\partial(\rho k)}{\partial t}+\frac{\partial\left(\rho u_j k\right)}{\partial x_j}=\rho P-\beta^*\rho\omega k+\frac{\partial}{\partial x_j}\left[(\mu+\sigma_k\mu_t)\frac{\partial k}{\partial x_j}\right] \tag{5.1}$$

$$\frac{\partial(\rho\omega)}{\partial t}+\frac{\partial\left(\rho u_j \omega\right)}{\partial x_j}=\frac{\gamma}{\nu_t}P-\beta^*\rho\omega^2+\frac{\partial}{\partial x_j}\left[(\mu+\sigma_\omega\mu_t)\frac{\partial k}{\partial x_j}\right]+2(1-F_1)\frac{\partial k}{\partial x_j}\frac{\partial \omega}{\partial x_j}\frac{\rho\omega 2}{\omega} \tag{5.2}$$

where ρ is density, t is the time, u_j and x_j are the velocity and position vectors respectively, μ_t is the eddy viscosity, ν_t is the kinematic eddy viscosity, γ is the intermittency factor, F_1 is a blending function and $\beta^*, \sigma_\omega, \sigma_k$ are constants. It is basically a combination of the $k-\epsilon$ model in the freestream and $k-\omega$ model near the walls of the geometry and is well suited for external aerodynamic flows around complex geometries and highly separated flows like airfoils at high angles of attack, which is most important in this thesis. STARCCM+ provides All y+, low y+ and high y+ wall treatments along with the $k-\omega$ SST model, however in this case the low y+ wall treatment is best suited and used since the wall y+ values must be kept around 1 to capture the boundary layer and calculate aerodynamic forces and coefficients accurately.

Due to the low speed nature of the flow which lie in the transition from the laminar to turbulent boundary layer region, transition prediction models such as the $\gamma-Re_\vartheta$ and turbulence suppression can also be used to accurately predict the onset of transition and calculate the aerodynamic coefficients. Test simulations were carried out initially for two different angles of

attack with and without the transition model and the differences in the aerodynamic coefficients were not significant enough. Also, the $\gamma - Re_{\vartheta}$ model is not accurate at predicting transition at high angles of attack. Considering these aspects, the resulting increased computational time and the presence of a propeller, it was decided to not incorporate the $\gamma - Re_{\vartheta}$ transition model in the current simulations.

5.2 Computational Domain and Mesh Generation

Based on the dimensions of the geometry and the complexity of the physics involved in the problem, a suitable computational domain must first be chosen to initiate the mesh generation process. The computational domain in this case for an external subsonic aerodynamics simulation must be such that the walls of the domain have zero or negligible effects on the flow field around the body/geometry being studied. After conducting several studies on computational domains and based on literature data available, a C shaped computational domain was considered to be the best choice to simulate freestream atmospheric conditions for an aircraft in flight as observed in Figure 18. Several different sizes for the domain were tested initially and finally a dimension of 8 m upstream and 10 m downstream from the nose of the fuselage was chosen for the current computational study. A test simulation was run to make sure the walls of the domain functioned effectively as free air and that there were no wall effects on the flow field around the DG808s geometry.

Figure 18: Computational domain for the DG808s CFD simulations

The C shaped – red color boundary of the domain was chosen to be a velocity inlet to simulate free air flight conditions and the vertical exit of the domain was chosen as a pressure outlet. To get results which were as accurate as possible to the AAA software and considering the

rotational region for the propeller, full symmetry of the aircraft was used rather than half symmetry even though it is computationally less expensive.

5.2.1 Mesh Generation

Once a suitable domain for the simulations was established, the next step was to setup the mesh for the geometry which forms the core of any CFD analysis. The accuracy of results and computational runtimes are major factors which are influenced by the mesh. One of the first decisions to be made was the selection of the type of mesh. Based on literature data and information available in the documentations of STAR-CCM+, polyhedral mesh was chosen over the trimmed cell mesher since it is known to perform better in regions with rotation and when aerodynamic coefficients are of importance. However, the polyhedral mesher took more CPU time while meshing when compared to the trimmed cell mesher since the polyhedral mesher always attempts to generate a conformal mesh. After a mesher was selected, several meshes were generated with different mesh parameters before finalizing a set of parameters as listed in Table 8. Default values were used for the parameters not mentioned in the table. As opposed to having regions of refinement around areas of importance, a small base size and slow growth rate was used so that cells on the surface and around the geometry were fine enough to capture

Table 8: Final mesh parameters in STAR-CCM+

Mesh Parameter	Corresponding Values
Base size	0.005 m
Minimum Surface size	12.50%
Surface curvature	100
Surface growth rate	1.15
Number of prism layers	20
Mesh density	0.6
Volume growth rate	1.2

aerodynamic data accurately. The prism layer near wall and total thickness were calculated based on the speeds being simulated and it was made sure that the wall y+ values were around or below 1.0. Using custom curve controls, mesh refinements were carried out on the leading and trailing edges of the lifting surfaces such as the wings, horizontal and vertical tails.

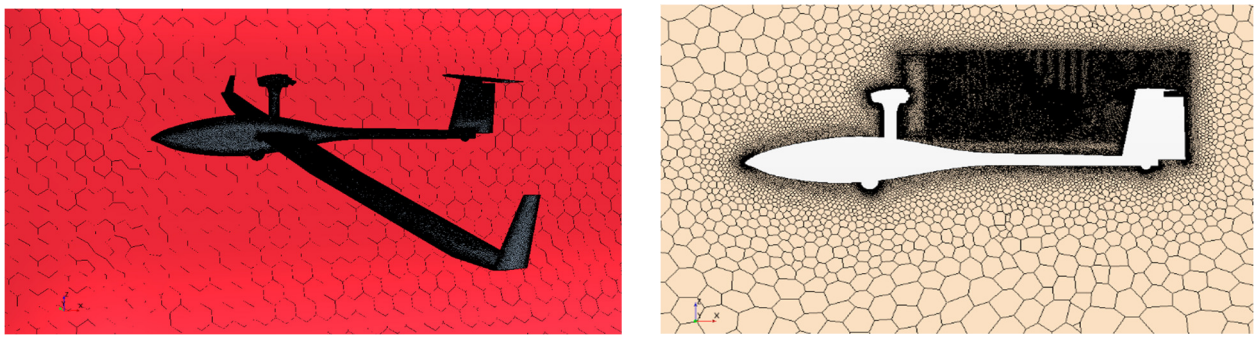

(a) (b)

Figure 19: Polyhedral mesh on the DG808s (b) Sectional view of the mesh refinement region between the propeller and horizontal tail

To accurately capture the propeller slipstream effects on the empennage of the aircraft, a wake refinement region leading from the propeller to the tail was incorporated where the cells were 50 % of the base size in terms of refinement as can be observed in Figure 19(b).

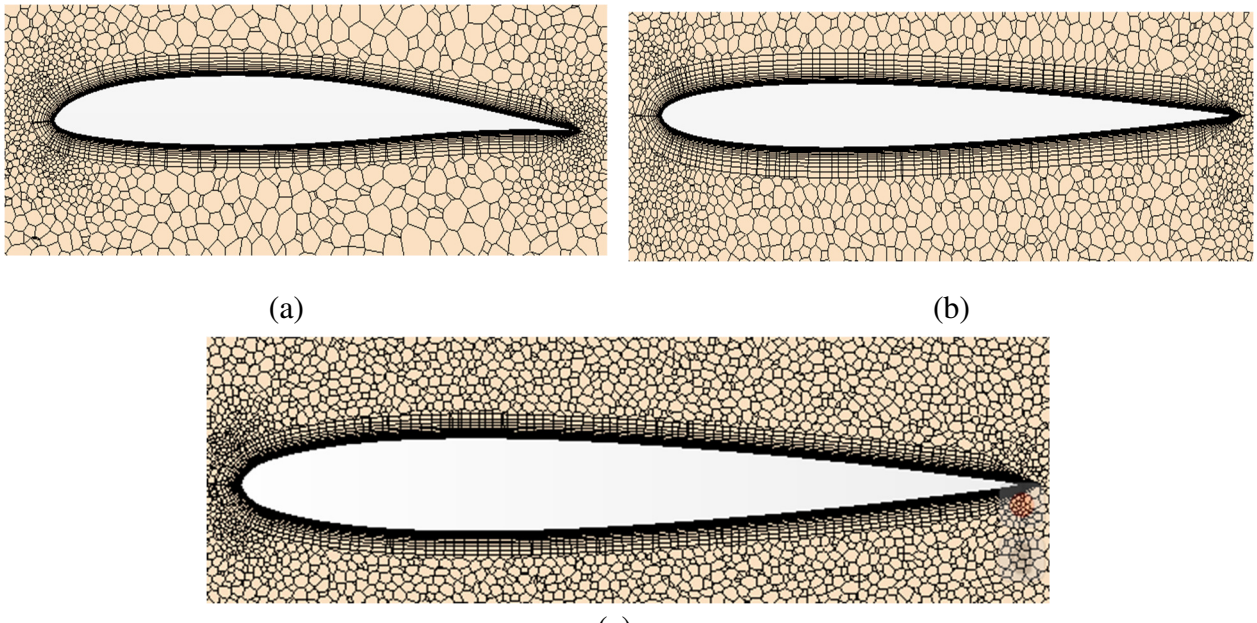

(a) (b)

(c)

Figure 20: Sectional view of the prism layers on (a) Wing (b) Horizontal tail (c) Vertical tail

Each time a mesh was generated, a full mesh diagnostic report was run to make sure metrics such as cell quality, face validity, volume change and skewness angles were < 0.01, 0.9 - 1.0, < 0.001 and < 85 degrees respectively.

5.2.2 Mesh Generation for Rotational Domain

To accurately model the propeller rotation which is the major crux of this thesis, a Rotating Reference Frame approach was used wherein the flow around the propeller is rotated rather moving the cells in the mesh as in the case of the Rigid Body Motion (RBM) model. A document laid out by CD-ADAPCO for the rotation modeling [49] was followed. The cylindrical domain for the rotating region was subtracted from the stationary region of the whole domain and was split into upstream, downstream and surrounding boundary conditions. Mixing plane interfaces were used at all the boundaries which essentially meant that the flow characteristics were transferred from the rotating region to the stationary region at the interface. A cell refinement of 50% base size was used for all the cells inside the rotating region for accuracy along with leading and trailing edge refinements for the propeller blades. The rotational domain with the propeller is presented in Figure 21.

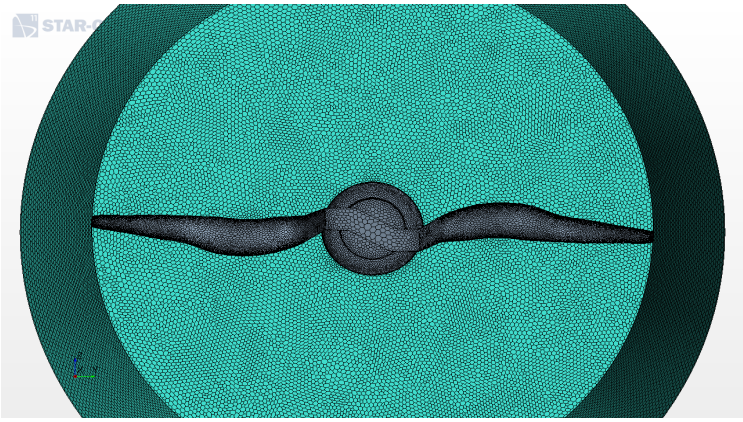

Figure 21: Polyhedral mesh inside the rotational domain for the propeller

On generation of the final meshes, the total cell count for the Poff case was around 12 million cells and 19 million cells for the Pon case. These cell counts were finalized after making sure no significant variations were present in the force coefficients for coarser and finer meshes as presented in Figure 22 for the Pon configuration. Base sizes used for the generation of the mesh

were varied to obtain global meshes of varying sizes. Since the propeller slipstream influence on the empennage of the aircraft was being studied here, lift coefficient of the horizontal tail was measured and compared.

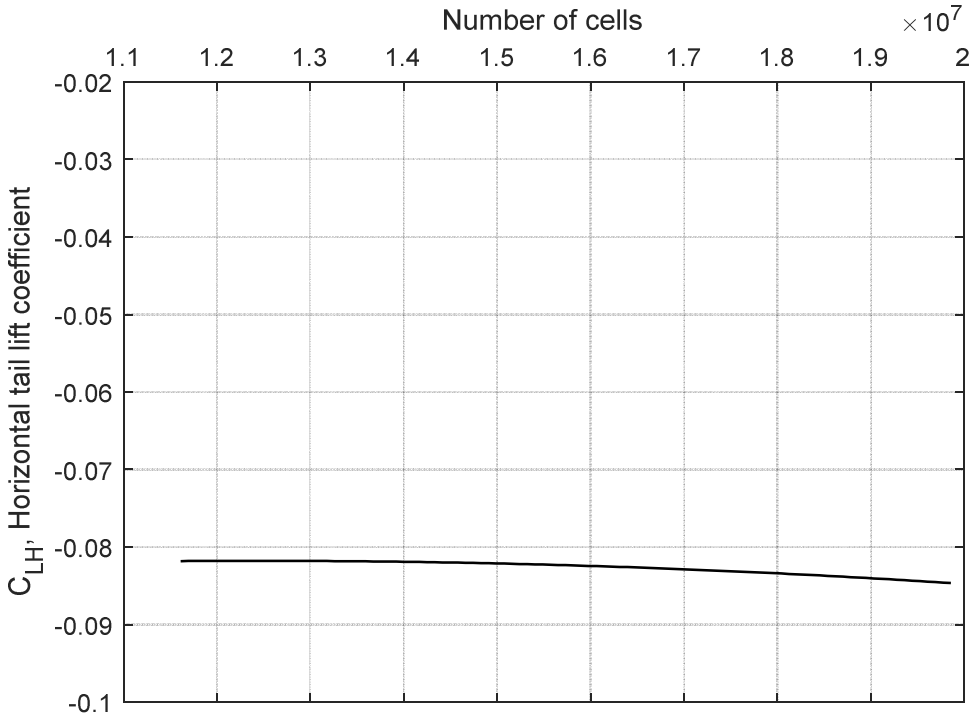

Figure 22: Grid convergence study

As observed from Figure 22, the lift coefficient for the final two mesh sizes did not vary by much, the difference being around 0.3% which was well within an acceptable range of 5% error. Hence, the final mesh size of approximately 19 million cells was chosen which was sufficient with the computing resources that were available. Cell sizes above these required extremely high mesh times which were not considered feasible due to the number of cases in the current study.

Chapter 6 . Results and Discussion

In this section, the results obtained from the various CFD simulations are presented followed by comparisons with respective data available from the AAA model. For the sake of organization, the analysis was split up into three different sections viz., longitudinal, lateral and simultaneous longitudinal-lateral analysis.

6.1 Longitudinal Directional Analysis

In this section, simulations carried out to investigate the impact of propeller slipstream on the horizontal tail, downwash angle and lift coefficient curves of the wing w.r.t angles of attack are presented.

Firstly, in order to check and validate the correctness and reliability of the models used in the CFD simulations, lift coefficients of the wing w.r.t angle of attack (α) were validated. A 2D calculation for the airfoil used in modeling the wing was carried out using the XFOIL [50] software. The lift coefficient vs angle of attack curve for a Reynolds number of approximately $2.2x10^5$ at the cruise flight conditions obtained from this calculation is presented in Figure 23(a).

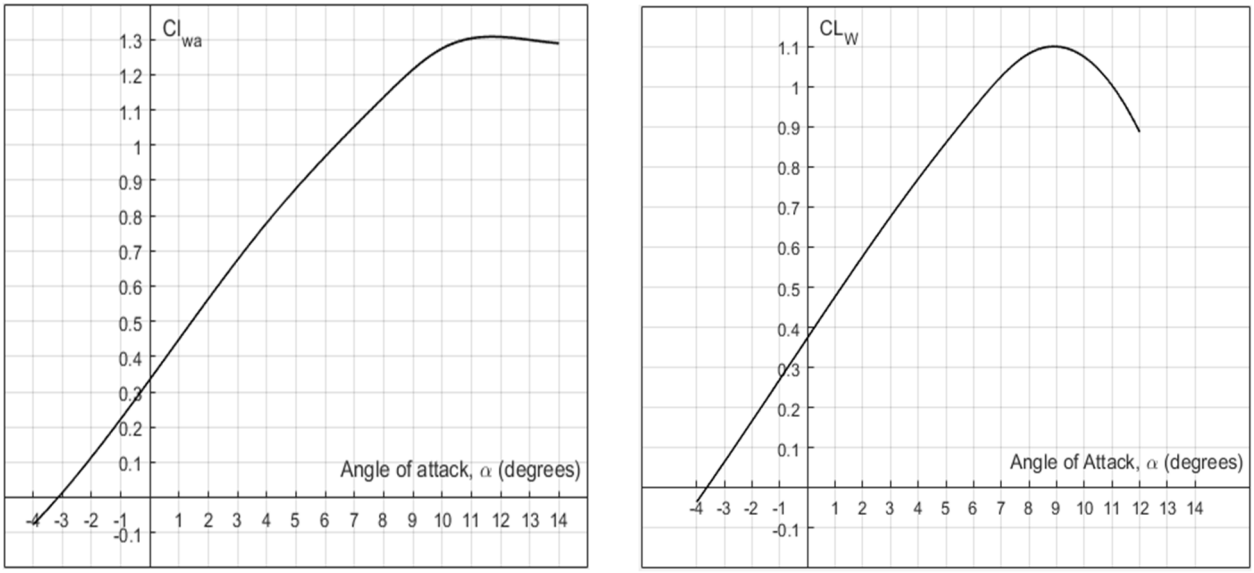

(a) (b)

Figure 23: Wing lift coefficient vs angle of attack curves at 18m/s (a) 2D airfoil - XFOIL (b) 3D wing - STAR-CCM+

The 2D lift curve slope (a_0) was then calculated from the curve using the slope formula:

$$a_0 = \frac{C_{l2} - C_{l1}}{\alpha_2 - \alpha_1}\ deg^{-1} \tag{6.1}$$

where, C_{l2} and C_{l1} are the lift coefficients of the airfoil at two different points along the y axis and α_2, α_1 are the corresponding angles of attack along the x axis. From the 2D lift curve slope (a_0) obtained above, the corresponding lift curve slope in 3D was then calculated using the conversion formulated in the thin airfoil theory [51] as mentioned in Equation (6.2).

$$a = \frac{a_0}{1 + \frac{57.3 * a_0}{\pi * AR * e}}\ deg^{-1} \tag{6.2}$$

where, AR is the wing aspect ratio which is 25.89 in the current case and e is the Oswald efficiency factor for the wing which is typically around 0.85 – 0.95. With the appropriate 3D lift curve slope in hand, the lift curve slope for the lift coefficient vs angle of attack curve of the wing obtained from the CFD simulations for a Poff flight as indicated in Figure 23(b) was then calculated using Equation (6.1). The resulting value was in close comparison to that calculated using the thin airfoil theory [51], with a negligible error of 6.52% which can be attributed to the several assumptions made in formulating the equations in the thin airfoil theory. Also, as expected XFOIL [50] overpredicts the stalling angle of attack of the airfoil which in theory should always be higher than that for the wing. These calculations and results confirmed the correctness of the models used in CFD and thus similar models and approach were used in the further simulations.

Once the validity of the models was established, comparative studies with the AAA software was carried out. According to Equation (3.4) as mentioned in [6], for a flight in the incompressible flow regime (M = 0), the downwash angle and the downwash gradient were assumed to be constant. To study this, the Poff flight was simulated in STAR-CCM+ at three different speeds: 14m/s, 18 m/s and 22 m/s which are the minimum, cruise and maximum flight speeds respectively within the incompressible flow region for DG808s. The lift vs angle of attack curve for the horizontal tail at the corresponding speeds are as indicated in Figure 24. The

downwash angle ε_0 being studied here is measured from the curve as the angle of attack at zero lift.

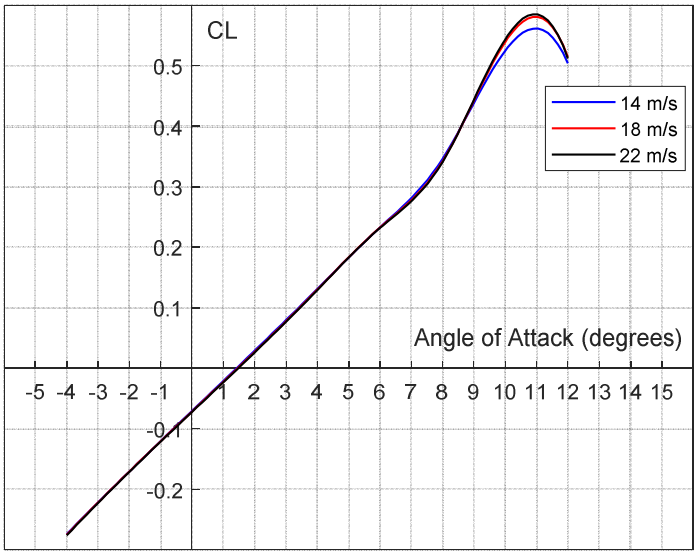

Figure 24: Horizontal tail lift coefficient vs angle of attack curve for different velocities and Poff configuration - STAR-CCM+

As observed in Figure 24, all three curves almost overlap each other and the only difference is seen in the measured maximum lift coefficient. The downwash angle at airplane zero angle of attack (ε_0) is measured to be approximately 1.3 degrees contrary to the 0.6 degree prediction by AAA as listed in Table 9. The angle however remains constant with variations in flight speeds which confirms the relations in [6] and Equation (3.4) that the downwash angle/gradient is independent of the flight speed in the incompressible flow region. To put the downwash angle estimation in a clearer perspective, simulations were carried out for an isolated horizontal tail wherein zero angle of attack produced a lift coefficient very close to zero as expected for a symmetric lifting surface, indicated in Figure 25.

Similar simulations were then carried out for the Pon configuration presented in Figure 25 with a rotation speed of 6500 RPM. As compared to what had been predicted by the AAA model and the assumptions made in [6], interesting results were obtained. The downwash angle at the

airplane zero angle of attack increased to approximately 2.2 degrees from the previous 1.3 degrees that had been obtained for the Poff condition, an increase of 70%.

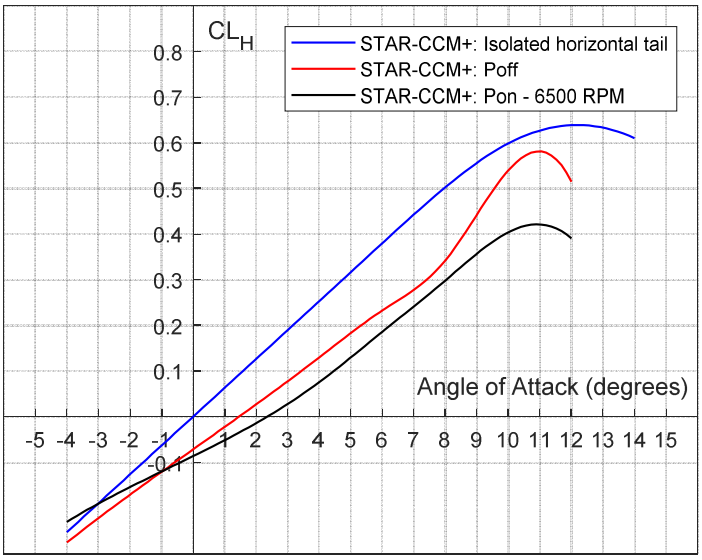

Figure 25: Horizontal tail lift coefficient vs angle of attack curve at 18m/s and different configurations - STAR-CCM+

A velocity magnitude contour at the root section of the aircraft for the Pon configuration was captured to check the maximum velocity in the propeller slipstream as observed in Figure 26. From the figure, it is clear that the maximum velocity in the slipstream is approximately 30.5 m/s which still falls under the incompressible flow regime.

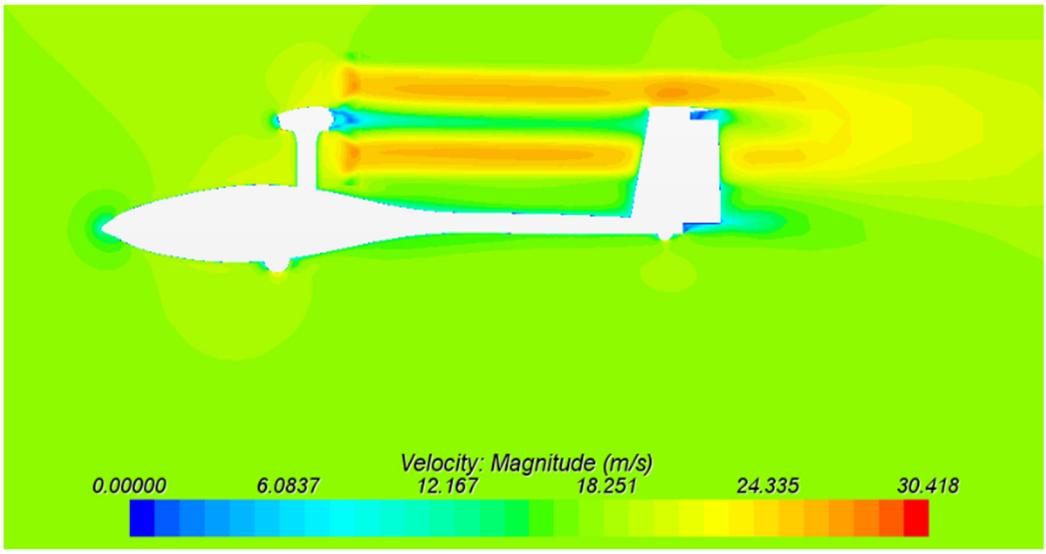

Figure 26: Sectional view of the velocity magnitude contour at 18 m/s and 6500 RPM - STAR-CCM+

Table 9: Downwash estimations: AAA and STAR-CCM+

Parameter	AAA	STAR-CCM+: Poff	STAR-CCM+: Pon – 6500 RPM
ε_0 (degrees)	0.6	1.3	2.2

As observed, when the slipstream effects due to a propeller was introduced variations in ε_0 were observed and hence it did not remain constant. This meant that the assumptions in Equation (3.4) and in [6] did not hold good for the DG808s. Due to the unconventional propeller configuration on the DG808s, the equation fell short in estimating the slipstream effects which explains the underestimation by AAA. Further, the assumption of the downwash gradient being constant needs to be investigated. Data in Figure 25 however, confirms the findings of [18] – [20] wherein the aerodynamic coefficients of the lifting surface decreased for regions within the slipstream with a resulting increase in downwash angle. Probes were placed on the maximum thickness points at 22 equidistant sections along the span of the horizontal tail to measure the axial velocity magnitudes. A flight speed of 18m/s and 6500 RPM propeller rotation was simulated. It is observed from Figures 27 and 28 that for the DG808s, approximately 70% of the horizontal tail is covered directly in the propeller slipstream which explains the overall decrease in aerodynamic coefficients and increase in downwash angle.

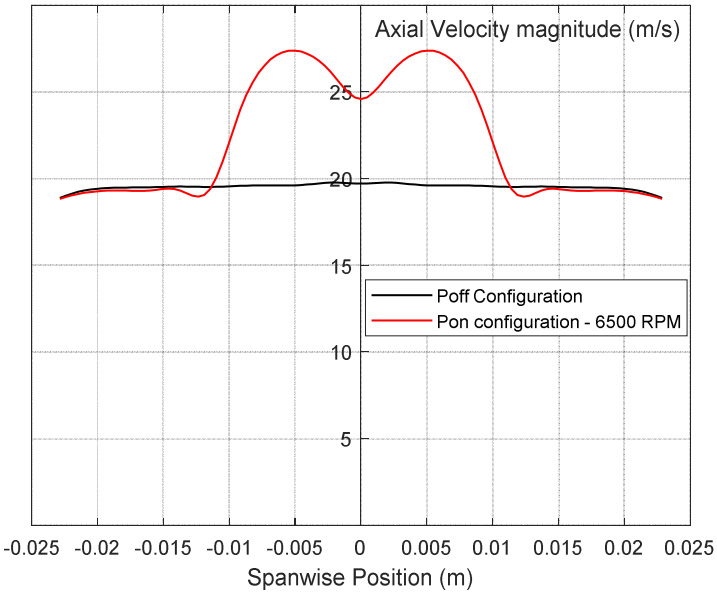

Figure 27: Axial velocity magnitude along the span of horizontal tail at 18 m/s - STAR-CCM+

To further support the results obtained and to make comparisons with data presented in [18]-[20], tangential velocity magnitudes near the horizontal tail section for both the Poff and Pon configurations were measured. The velocity magnitudes were measured at similar points as in Figure 27.

A strong component of the velocity in the tangential direction within the slipstream relative to the axial freestream velocity is observed. This tangential velocity component mixes with the vortex sheet generated from the wing, reduces the local angle of attack and creates a strong downward component which influences the horizontal tail thereby leading to a reduction in the aerodynamic characteristics of the tail and a simultaneous increase in the downwash. A part of the horizontal tail on the right side from the root section when viewed from the top of the aircraft seems to be covered with velocity components in the upward direction resulting in decreased downwash. This confirms findings of [18] wherein the horizontal tail was split up into two sections of opposing behaviors. As observed from Figure 29 and established earlier, a higher percentage of the horizontal tail (70%) appears to be covered in the increased downwash section with strong downward velocity components thereby resulting in an overall increase in downwash.

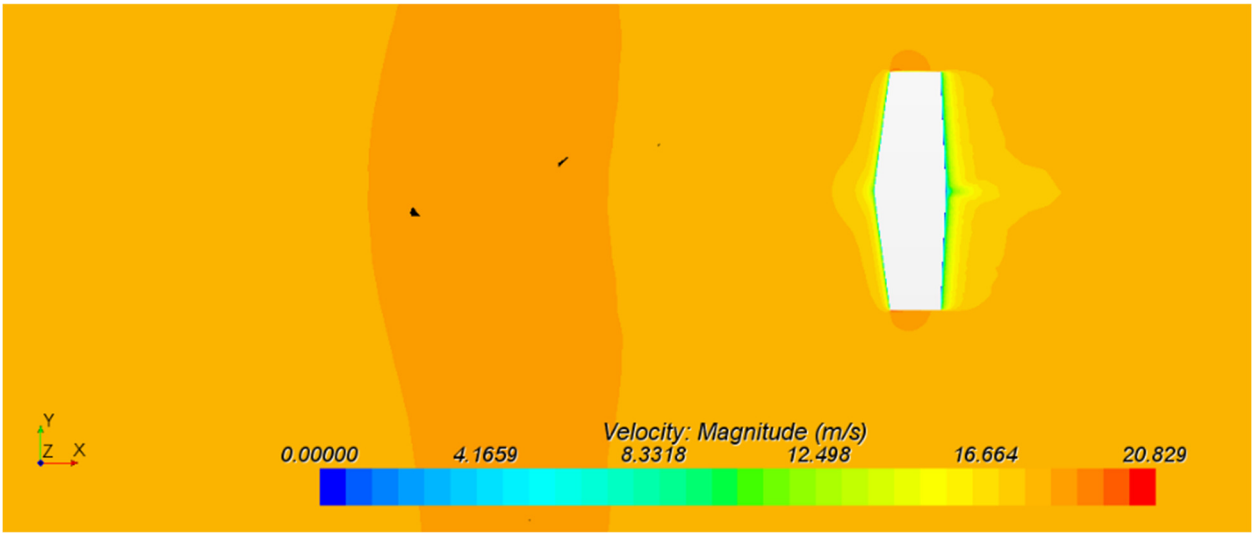

(a)

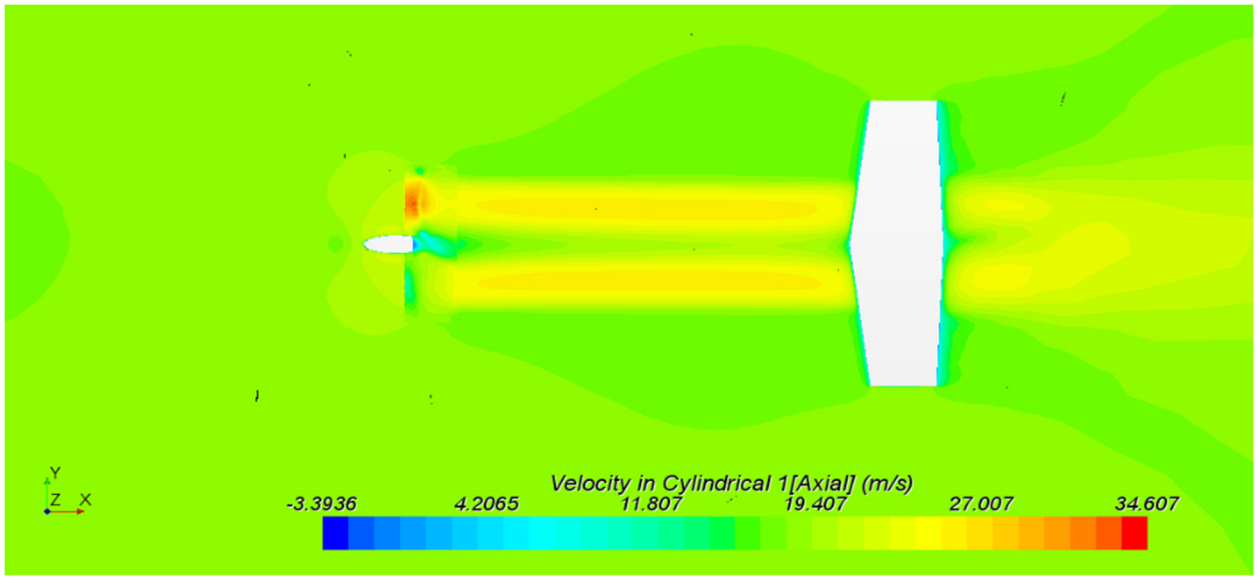

(b)

Figure 28: Top view of the velocity magnitude contours over the horizontal tail at 18 m/s (a) Poff configuration (b) Pon configuration - 6500 RPM - STAR-CCM+

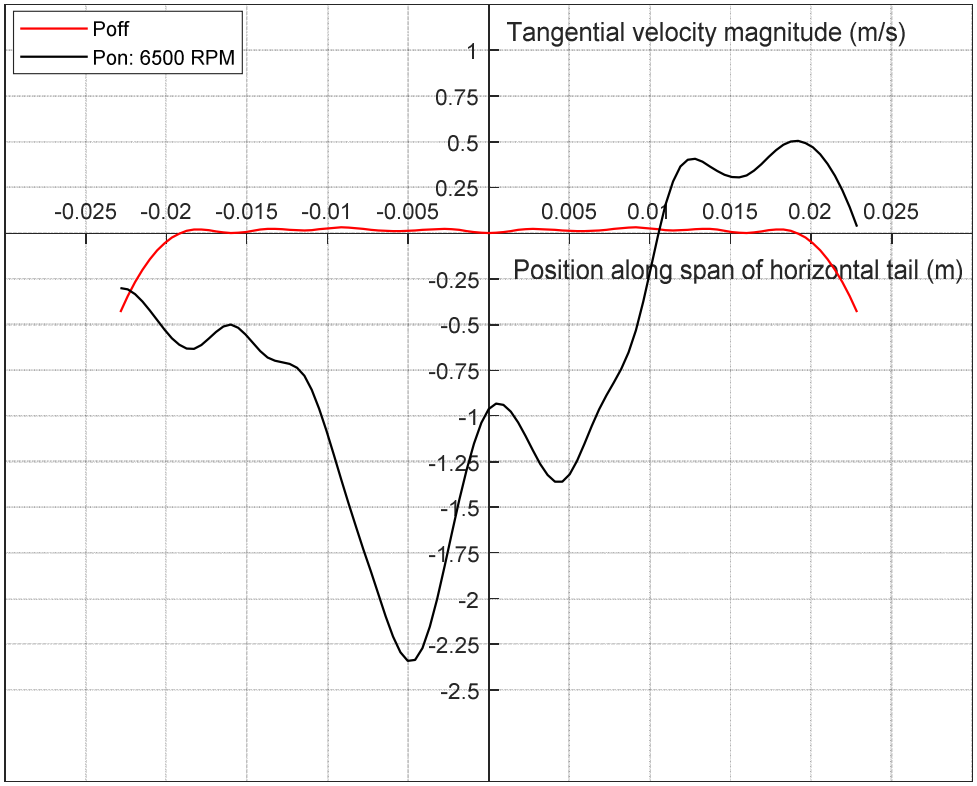

Figure 29: Tangential velocity magnitudes at the maximum thickness point over the horizontal tail at 18 m/s & 6500 RPM - STAR-CCM+

Another important observation from Figure 29 is the asymmetric nature of the tangential velocity magnitudes. The horizontal tail is affected non-linearly in the wake generated by the upward and downward components of the rotating propeller. This means the local angles of attack at the horizontal tail kept varying for different positions along the span.

For a better understanding of the behavior of the horizontal tail in the slipstream, the rotational speed of the propeller was increased to the maximum operating range of 10,000 RPM as presented in Figure 30. As observed, the lift coefficient of the horizontal tail reduced as compared to 6500 RPM until the linear part of the curve with an increase in ε_0 due to stronger downward velocity components on the horizontal tail as presented in Figure 31. After this, around 4 degree angle of attack the lift coefficient curve behaves extremely nonlinear wherein the lift coefficient increases abruptly up to the stalling angle of attack and then reduces with an overall reduction in the maximum lift coefficient. This provides evidence that the aerodynamic performance of the horizontal tail in the slipstream is a direct function of the propeller RPM.

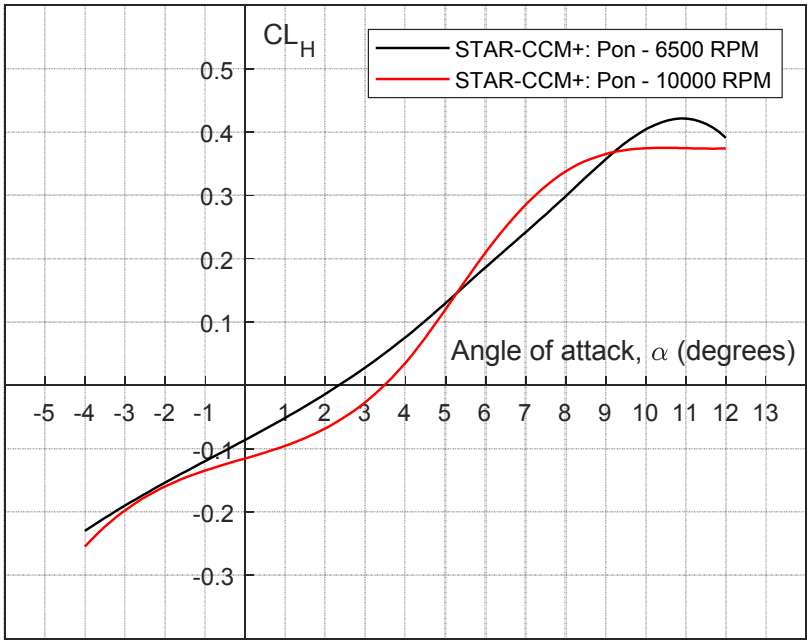

Figure 30: Horizontal tail lift coefficient vs angle of attack curve at 18 m/s and different RPM's

Table 10 lists the percentage increase in the zero angle of attack downwash angle (ε_0) from 6500 RPM to 10000 RPM. An increase of approximately 50% is measured which is quite significant which AAA falls short in estimating for the DG808s. Downwash estimations obtained for the 6500 RPM and 10000 RPM Pon cases are of major significance in determining the longitudinal stability and control derivatives of the aircraft as explained in Section 3.2. Not accounting for the extremely large variations observed due to the slipstream could make the system highly unstable leading to early stall of the horizontal tail.

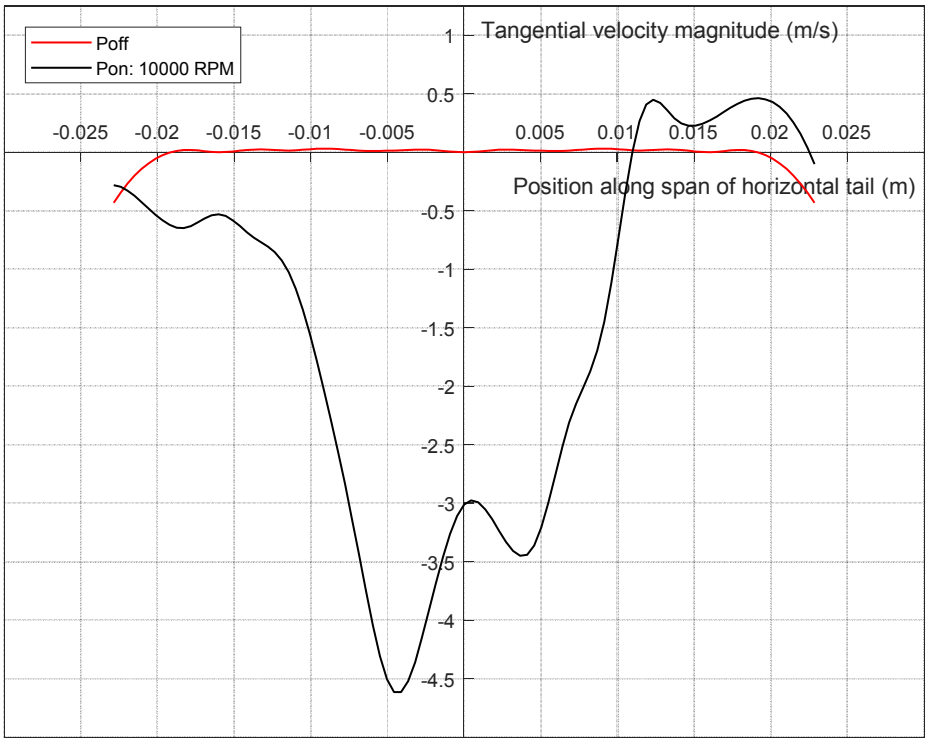

Figure 31: Tangential velocity magnitudes at the maximum thickness point over the horizontal tail at 18 m/s & 10000 RPM - STAR-CCM+

To study the extent of non-linearity imposed on the horizontal tail by the propeller slipstream, numerical gradient of the lift coefficient w.r.t the angle of attack ($\frac{\partial C_{L_H}}{\partial \alpha}$) was calculated and is presented in Figure 32. For the isolated horizontal tail and the Poff cases, the gradient is linear until the linear part of the lift coefficient vs angle of attack curve after which the curve exhibits non-linearity in the stalling region of the horizontal tail. For the Pon cases however, the curve exhibits non-linearity even at low angles of attack. As the RPM of the propeller is increased

to 10000, the nonlinearity increases and it is extremely difficult to assume a certain range of linearity. This supports findings in Figure 30 and is due to the varying local angles of attack for the horizontal tail at different locations in the slipstream. However, a detailed study needs to be conducted in this regard to make valid conclusions.

Table 10: Percentage increase in ε_0 of Horizontal tail for propeller RPM variation

Configuration	ε_0 (degrees)	Percentage Increase
Pon: 6500 RPM	2.2	50%
Pon: 10000 RPM	3.3	

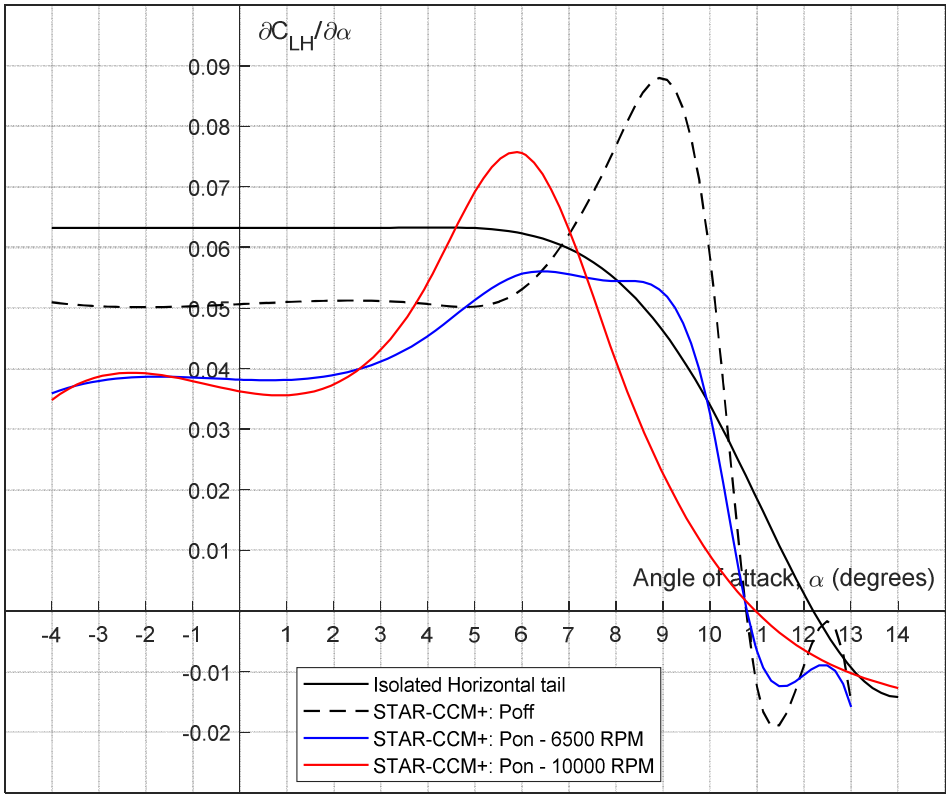

Figure 32: Numerical gradient of the horizontal tail lift coefficient with angle of attack at 18m/s and different configurations

To conclude the longitudinal analysis, propeller slipstream effects on the forward lifting surface viz., the wings was measured at the cruise flight speed of 18 m/s and the corresponding lift

coefficient vs angle of attack curve is presented in Figure 33. It is observed that regardless of the aircraft configuration (Poff or Pon), the lifting characteristics of the wing seem to be majorly unaffected by the swirling components in the propeller slipstream. Changes if any are negligible to be considered significant. However, this conclusion is based on the current aircraft with an unconventional propeller location and hence it cannot be generalized.

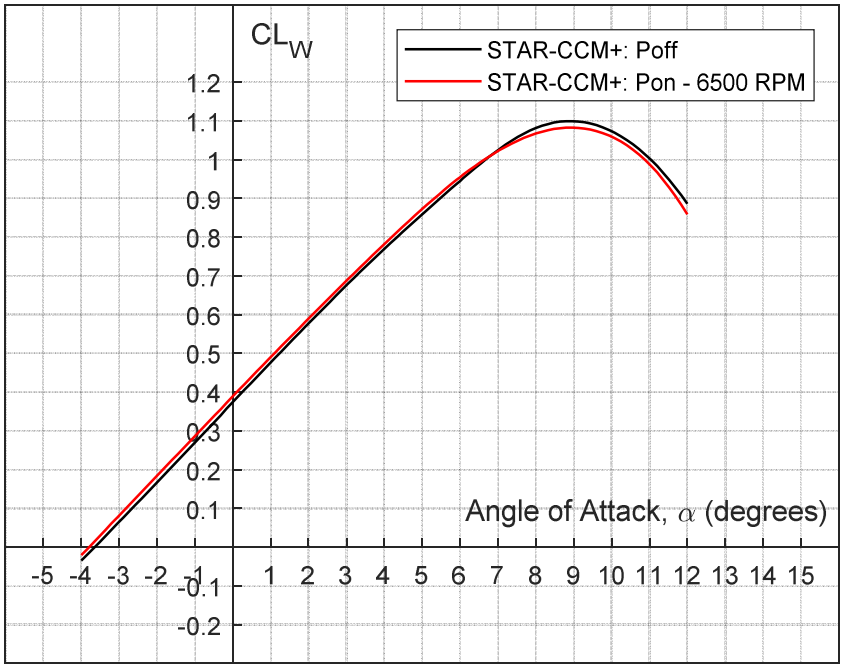

Figure 33: Wing lift coefficient vs angle of attack at 18m/s and different configurations

6.1.1 Comparison of Longitudinal Directional Analysis with Flight Test Data

A comparison of performance data from STAR-CCM+ in the longitudinal direction with the flight test data was carried out to test the correctness of the CFD estimations. C_{LO} which is the lift coefficient at zero angle of attack for the whole aircraft was compared as presented in Figure 34. Since steady state simulations were carried out using STAR-CCM+, variations with time could not be estimated and hence the straight horizontal line w.r.t time. ANN represents the Artificial Neural Network technique and LSE is the Least Squares Estimation method for system identification carried out by the Flight Systems Team at The University of Kansas. As observed from the figure, the data generated by STAR-CCM+ is overpredicted ($\approx 30\%$) as compared to the system identification data. This could be due to the various factors that were not considered in the CFD modeling such as gaps in the airframe i.e., control surfaces, propeller RPM discrepancies

between CFD and flight tests, flight speed discrepancies and variations w.r.t time. CFD induced factors such as turbulence model selection, numerical diffusion errors and mesh sizes could have contributed to the discrepancy too. However, the data was considered sufficient to establish the correctness of the CFD modeling. For a more accurate comparison, the above-mentioned factors should be taken into account.

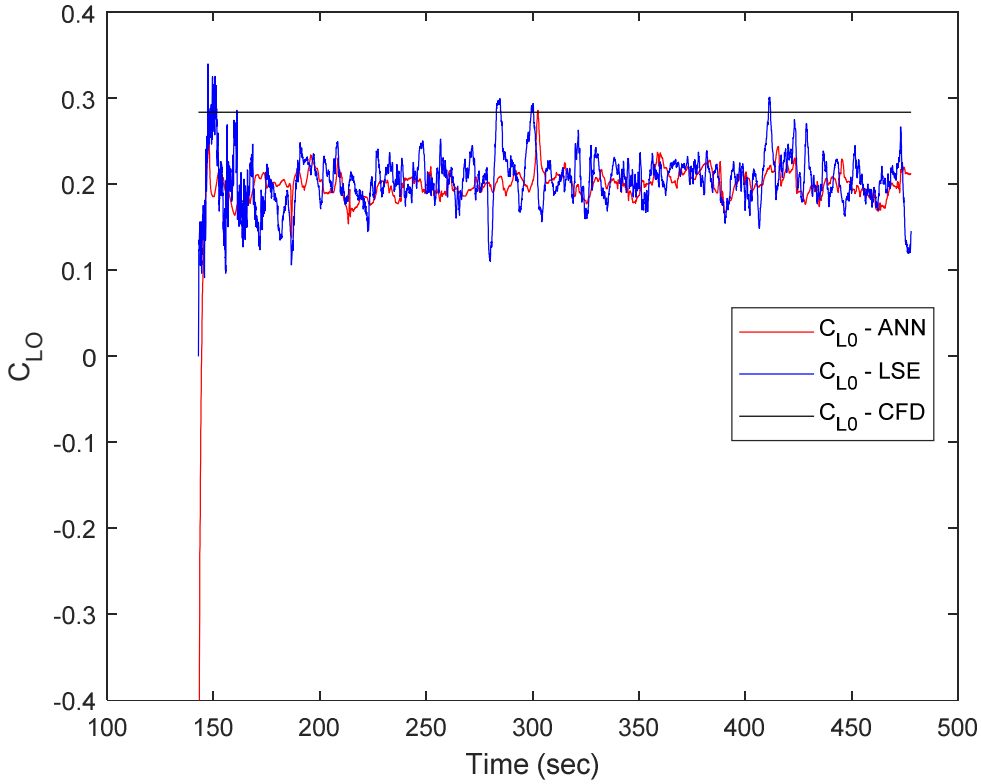

Figure 34: Zero Angle of attack lift coefficient comparison with System Identification data

6.2 Lateral Directional Analysis

After establishing the longitudinal behavior of the tail section in the propeller slipstream, lateral directional analysis was carried out to establish the aerodynamic behavior of the vertical tail, sidewash angle and performance characteristics for variations in sideslip angle all of which will be presented in this section.

To first establish baseline performance data for the vertical tail, CFD simulations were initially carried out for an isolated vertical tail as used in the full aircraft configuration by eliminating the fuselage, wing, horizontal tail and other components. The side force coefficient generated by the vertical tail which is nothing but the lift generated by the vertical tail in the lateral

direction was measured. Once baseline data was established, side force generated by the vertical tail in the full aircraft configuration was simulated and a comparison of this data is presented in Figure 35.

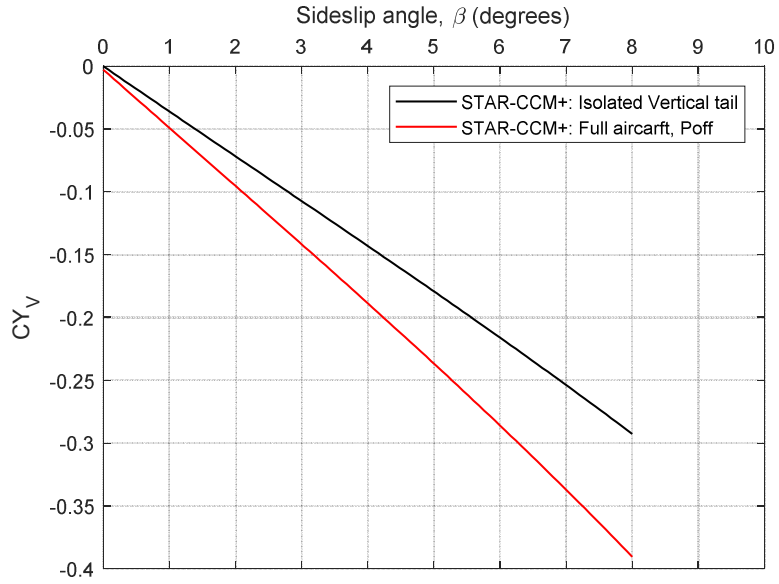

Figure 35: Vertical tail side-force coefficient vs sideslip angle at 18 m/s and different configurations

As observed from Figure 35, the side force coefficient C_{YV} generated by the vertical tail for the full aircraft - Poff configuration is relatively higher and the difference seems to increase with increase in sideslip angle β. This confirms the hypothesis stated in [5] about the component of side-force generated from the wing which adds on to the side-force generated by the vertical tail resulting in a higher side-force coefficient of the vertical tail. The hypothesis is formulated in Equation (6.3) below.

$$C_{Y_{wing}} = -C_{D_{wing}} \triangleq -C_{D_{parasite-wing}} \tag{6.3}$$

where, C_D is the parasitic drag coefficient generated by the wing. Table 11 lists the percentage contribution of different components of the aircraft to the vertical tail side force.

Table 11: Maximum percentage contribution of different components of the aircraft to the vertical tail side force

Sideslip angles	Maximum percentage contribution
Low - Moderate angles (0-4 degrees)	31.90%
Moderate - High angles (4-8 degrees)	33.50%

To validate the side force data generated for the Poff configuration, the side force coefficient values from the AAA model were compared with, as observed in Figure 36. The sideslip angle was maintained to a maximum of +10 degrees. According to sign convention as mentioned in Section 3.3, left yaw of the nose when viewed from the top is considered as positive sideslip angle and vice versa. It is clear from the plot that the data generated by the CFD simulations are in close agreement with that generated by AAA. The percentage discrepancy appears to increase with increasing sideslip angles. However, the maximum discrepancy at +10 degrees β is still in the acceptable bounds. This could be accounted to the ability of STAR-CCM+ to accurately capture the vortices generated from the wing and the additional component of the side-force from the wing as mentioned in Equation (6.3).

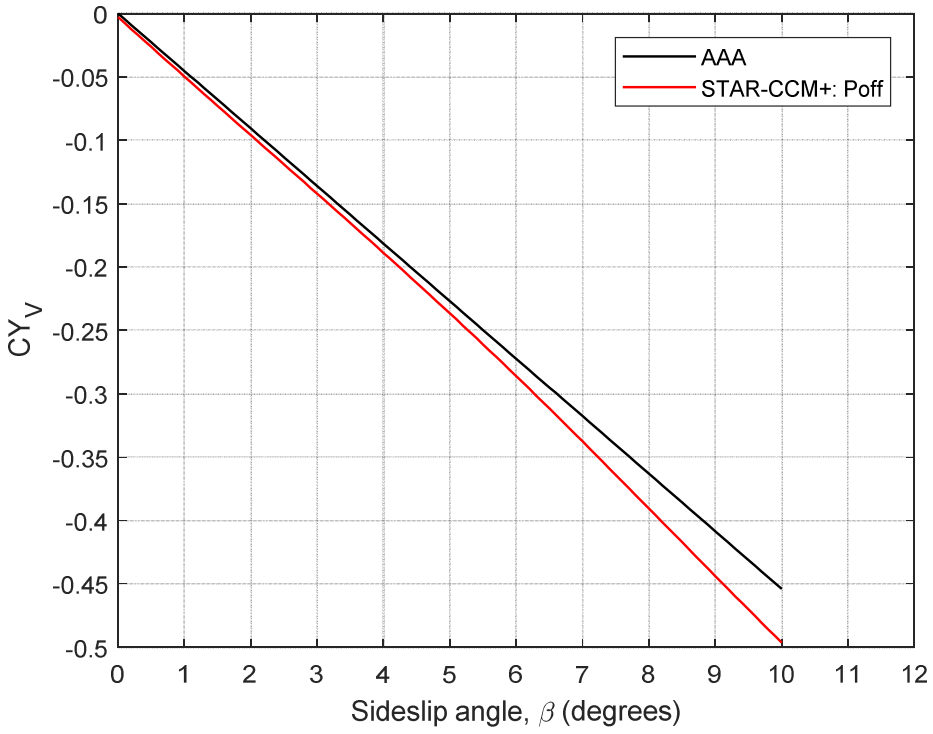

Figure 36: Vertical tail side-force coefficient vs sideslip angle at 18 m/s

Table 12 lists the percentage discrepancies between the data obtained by STAR-CCM+ and AAA. All percentages were calculated by using AAA data as the reference.

After establishing performance data for the Poff configuration of the vertical tail, the next step was to study the behavior of the vertical tail in propeller slipstream i.e., Pon configuration.

Two different rotational speeds of the propeller viz., 6500 and 10,000 RPM were simulated. The data obtained is presented in Figure 37.

Table 12: Maximum percentage discrepancies in C_{YV} between STAR-CCM+ and AAA for Poff configuration

Sideslip angles	Maximum percentage discrepancy
Low - Moderate angles (0-5 degrees)	4.63%
Moderate - High angles (5-10 degrees)	9.36%

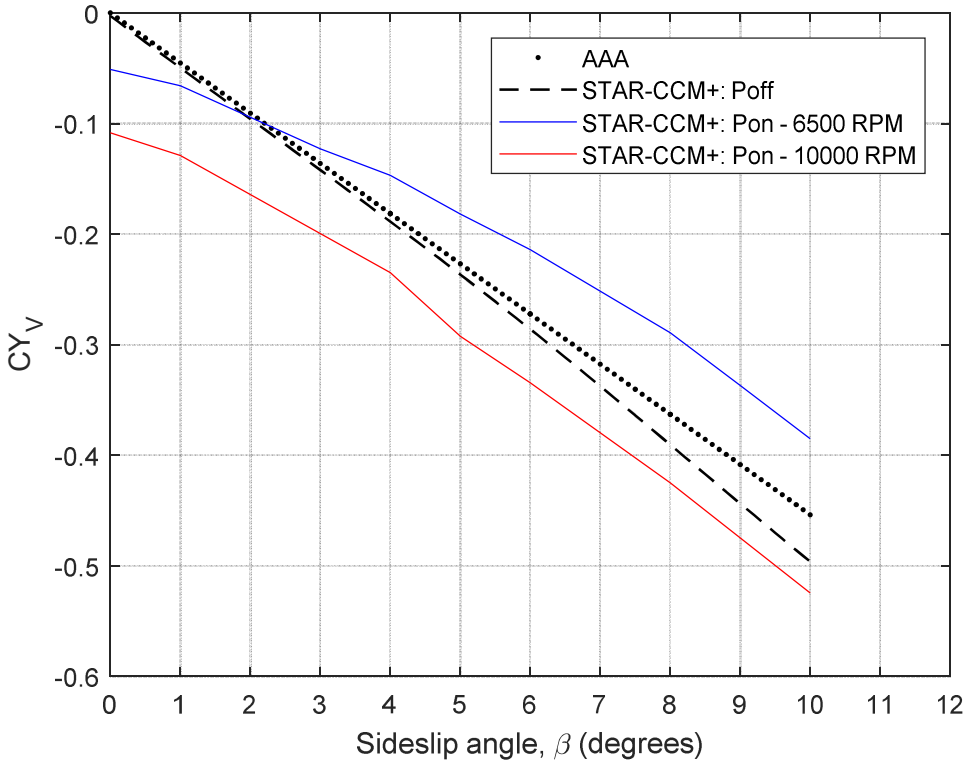

Figure 37: Vertical tail side-force coefficient vs positive sideslip angle at 18m/s and different RPM's

The most significant change observed is the nonzero nature of the zero sideslip side force coefficient and sidewash angle represented by σ_0. Instead, it is a large value. This meant that the assumption about σ_0 being negligible made in equation (3.11) did not hold good for the DG808s. Also, a dependency of C_{YV} on the propeller RPM is observed as indicated by the higher zero-sideslip C_{YV} for the 10,000 RPM case. Closer inspection revealed a nonlinear impact of four curves hence establishing the nonlinear behavior of the vertical tail in slipstream as opposed to the linear assumption in [6].

For a complete behavioral analysis, the aircraft was placed at negative sideslip angles and the corresponding data generated is observed in Figure 38. Since the DG808s being studied here is a symmetric aircraft with a symmetric airfoil used in the design of the vertical tail, a symmetric curve for the side-force coefficient generated by the vertical tail was expected and is confirmed by the curves presented for the AAA model and the CFD data for Poff flight. The curves for the Pon

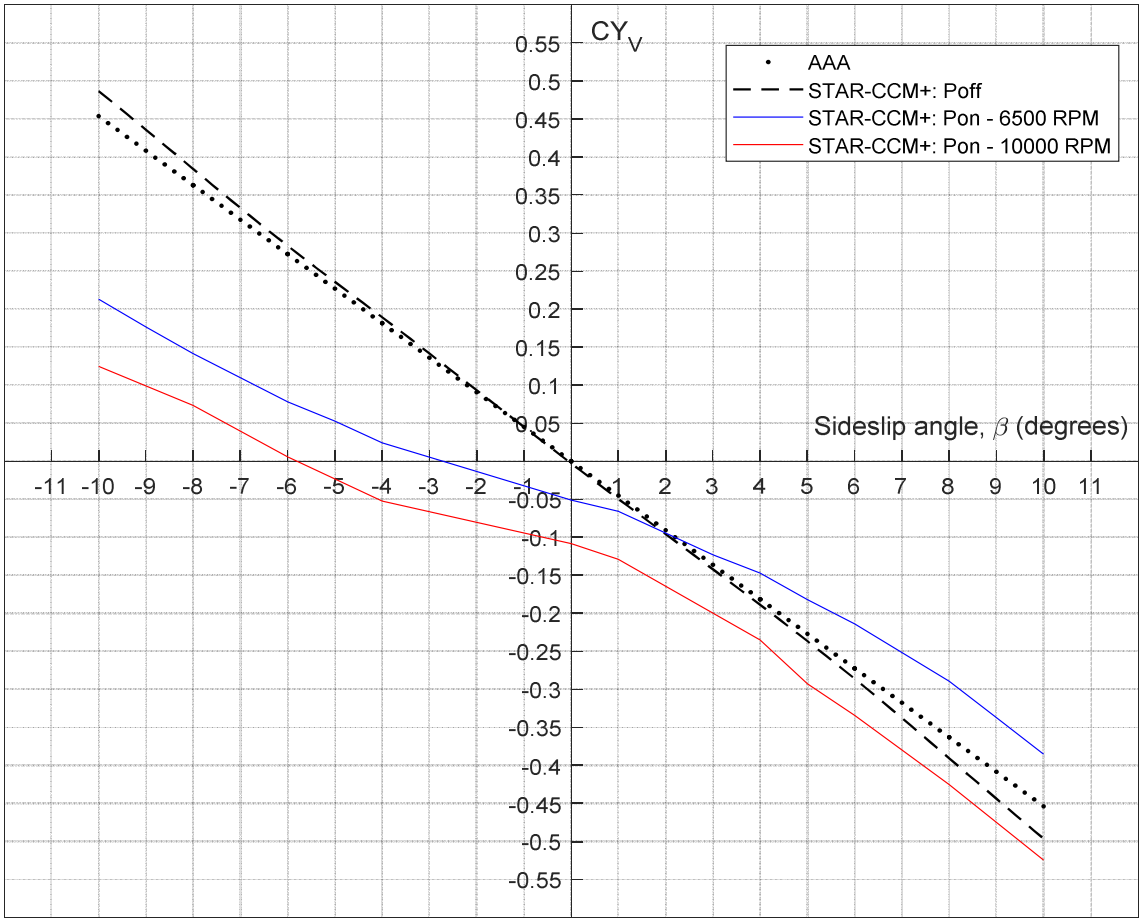

Figure 38: Asymmetric nature of the vertical tail side-force coefficient vs positive and negative sideslip angles at 18 m/s

cases however, show an asymmetric nonlinear behavior due to the propeller slipstream and this behavior is found to be a direct function of the direction of propeller rotation (clockwise rotation in this case) and RPM. A good explanation to this behavior can be established from the theory presented in Section 3.3. Due to the clockwise nature of rotation of the propeller, natural tendency of the aircraft is to yaw towards the left i.e., a negative yawing moment where the vortices generated from the wing and those present in the propeller wake interact thus impacting the vertical tail performance. However, placing the aircraft at a negative sideslip angle with the same clockwise

rotation of the propeller counteracts with the natural tendency of the aircraft to have a positive sideslip due to the negative yaw which explains the relatively low side-force coefficient values of the vertical tail. Confirmation of this was provided by the large values of rudder deflection observed in the flight tests. Table 13 lists the percentage discrepancies in the zero sideslip side force coefficients of the vertical tail between the different propeller RPM configurations.

Table 13: Percentage increase in C_{YV} at zero sideslip for different propeller RPMs

Configuration	C_{YV} – Zero β	Percentage increase
Pon: 6500 RPM	-0.052	111.53%
Pon: 10000 RPM	-0.11	

Relatively large values for σ_0 were observed due to the propeller slipstream. An increase due to the variation in RPM confirmed a direct relation between σ_0 and propeller RPM. This meant that for the DG808s, the zero sideslip sidewash angle could no longer be considered negligible. Equations in [6] fell short in predicting σ_0 for the DG808s due to its unconventional location of the propulsion unit. Table 14 lists the percentage discrepancies in σ_0 due to propeller RPM.

Table 14: Percentage increase in σ_0 due to increase in propeller RPM

Propeller RPM	σ_0 (degrees)	Percentage increase
6500	-2.8	110.70%
10000	-5.9	

To record the extent of non-linearity, the side-force gradient $\frac{\partial C_{Y_V}}{\partial \beta}$ w.r.t the sideslip angle β ($C_{Y\beta}$) was calculated and the corresponding values were plotted against β as observed in Figure 39. The gradient from the AAA model is completely linear as per [6] and Equation (3.11). The curve for the CFD - Poff configuration although not completely linear, exhibits linearity up to moderate sideslip angles after which there is a nonlinear transition at higher sideslip angles. After the transition, the curve appears to attain linearity again. As explained in the earlier figures, this may be due to STAR-CCM+'s ability to capture flow phenomena induced due to the wing accurately. Thus, the overall behavior can be assumed linear as per assumptions in [6]. For the Pon

cases however, the behavior as observed is extremely nonlinear. It is impossible to derive even a single linear curve. For relatively low negative β, the curves for the two RPMs follow similar trends and peak at a maximum value but at regions other than this, the curves exhibit extreme nonlinearity. This extreme nonlinearity can be explained with the aid of vortex flows. The distribution of the vortex varies inversely with the distance 'r' from the core of the vortex. Since, the vortices come in contact with the vertical tail along different spanwise locations, the vortex strength at each location varies. This causes variations in local sideslip angles β experienced by the vertical tail in a nonlinear pattern thus explaining the extremely bizarre and nonlinear variation of the gradient curves. This is again a function of the propeller rotational orientation (clockwise) which causes local flow angles at the vertical tail to appear as a negative β. A counterclockwise propeller rotation would cause the curves to peak to a maximum at a relatively low positive sideslip angle β.

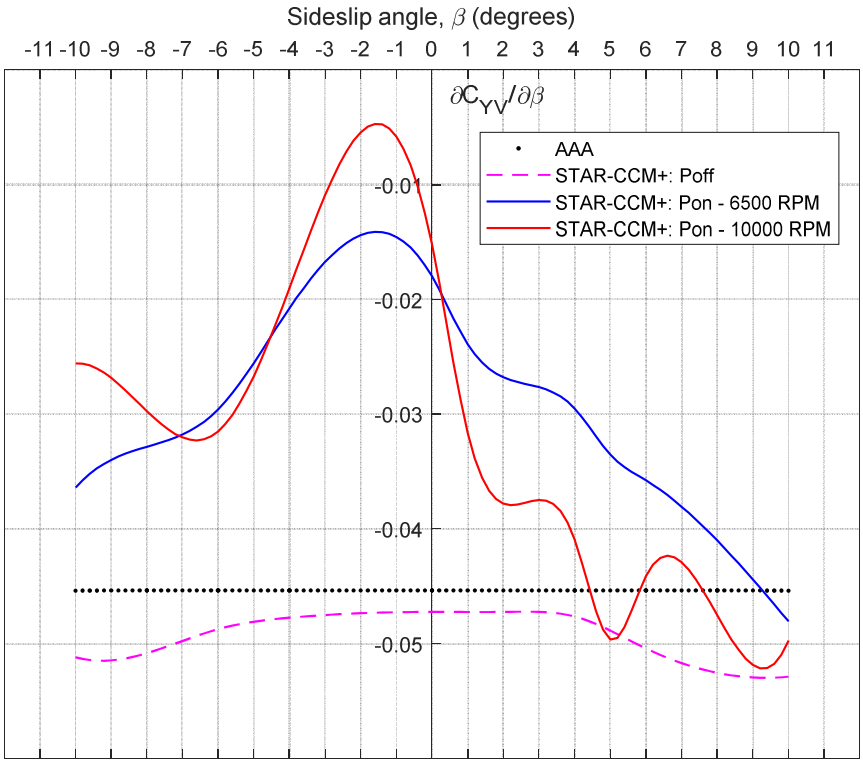

Figure 39: Numerical gradient of the vertical tail side-force coefficient with sideslip angle at 18 m/s

A detailed explanation of this can be found in [51]. However, further study needs to be conducted in this regard to provide stronger and valid explanations.

6.2.1 Comparison of Lateral Directional Analysis with Flight Test Data

To determine the validity of the side-force coefficient data of the vertical tail generated by STAR-CCM+, a comparison with the system identification data generated through flight tests was made. Unfortunately, no direct side-force coefficient data was available due to the lack of equipment needed to measure it, however an indirect correlation was established by comparing the rudder deflection angles required to maintain the aircraft at steady straight line flight. Table 15 lists the average rudder deflection angle observed in the flight tests.

Since the flight test data had a range of flight speeds, values corresponding and close to 18m/s only were chosen for comparison. According to sign convention when viewed from the top

Table 15: Average rudder deflection angle from flight test data

Flight speed	Parameter	Value (degrees)
18 m/s	Average rudder deflection	-0.7

of the aircraft, a rudder deflection towards the left is considered to be a positive rudder deflection which causes yaw towards the left and vice versa as shown in Figure 40. Y_V represents the side-force generated by the vertical tail. As explained in Section 3.1, for a clockwise rotation of the propeller as is the case in this study, natural tendency of the aircraft

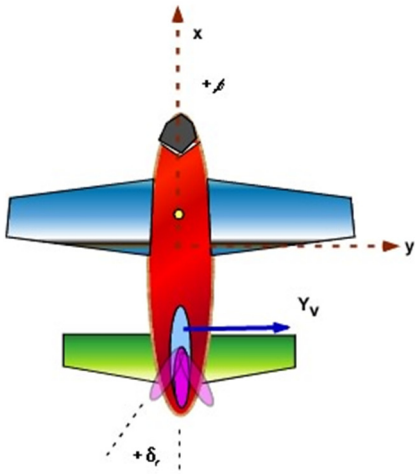

Figure 40: Sign convention for rudder deflection [46]

is to yaw towards the left i.e., a negative yawing moment, confirmed by the relatively high negative C_{YV} for zero sideslip as observed in Figure 37 and 38. This explains why the system needed some

amount of negative deflection to the rudder (right deflection) to allow the vertical tail to produce a higher side force, creating a counteracting yawing moment towards the right in order to level the aircraft to a steady state. This is the effect of σ_0 which is assumed to be negligible in [6]. This is however not the case for the DG808s and instead it is a large value. The relatively large discrepancies in the deflection angles however could be due to the variation in propeller RPMs as it was established that the side-force coefficient is a function of the propeller RPM in Figure 39.

6.3 Simultaneous longitudinal and lateral directional variations

The final part of this thesis presented in this section involved simultaneous variations of the angle of attack α and sideslip angle β of the aircraft. Aerodynamic characteristics of the vertical and the horizontal tail were measured in the propeller slipstream for a flight speed of 18 m/s. As per [6], variations in lateral directional flow angles have negligible effects on the longitudinal forces and moments and vice versa. Investigating the validity of this assumption for the DG808s when in propeller slipstream was the motivation behind this analysis.

Figure 41 indicates the lift coefficient vs angle of attack curve for the primary lifting surface viz., the wings. As observed and established earlier, the propeller slipstream has little to no effect on the performance of the wing due to it being in undisturbed freestream air. The variations in the lift coefficient were too small (within 5%) to be considered significant hence confirming the decoupling assumption in [6].

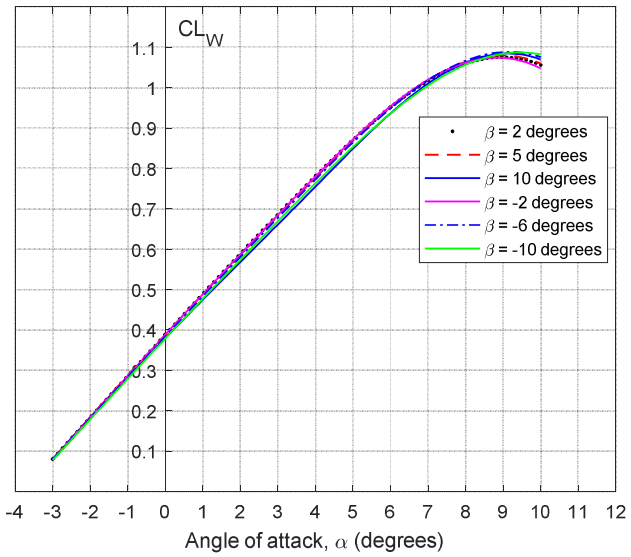

Figure 41: Wing lift coefficient vs angle of attack curve for different sideslip angles at 18 m/s and 6500 RPM - STAR-CCM+

Performance variations for the empennage section of the aircraft however had significant variations. The lift coefficient vs angle of attack curve of the horizontal tail for different sideslip angles and the two different operating RPM's of the propeller is presented in Figure 42(a-b). As observed from Figure 42(a-b), the variations in the lift coefficient are minimal for relatively small sideslip angles. A relatively large variation is observed for the -6 degree sideslip angle case for both the RPMs. The most significant change however is observed for high sideslip angles (-10 and +10 degrees). Linearity of the curve is no longer present indicating premature stall of the horizontal tail and its ineffectiveness at high sideslip angles and angles of attack. The decoupling assumption in [6] appears to not hold good for this configuration. This can be attributed to the extremely nonlinear mixing of the propeller slipstream, the freestream air and the vortices generated from the wing, affecting the flow over the horizontal tail. Another important observation is the curve for the -6 degree sideslip angle - 10000 RPM case. The ineffectiveness of the horizontal tail occurs much earlier as compared to the 6500 RPM case.

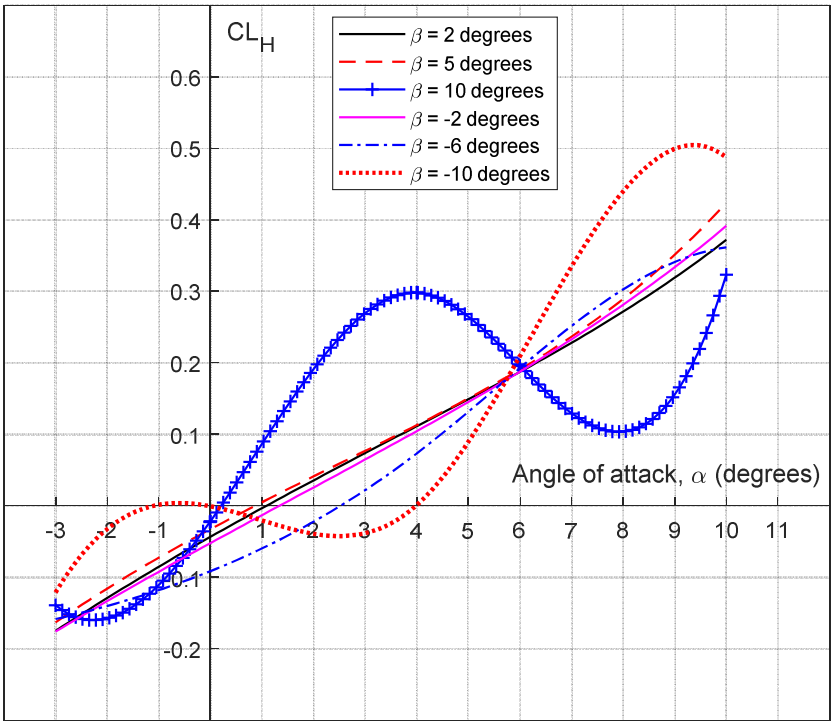

(a)

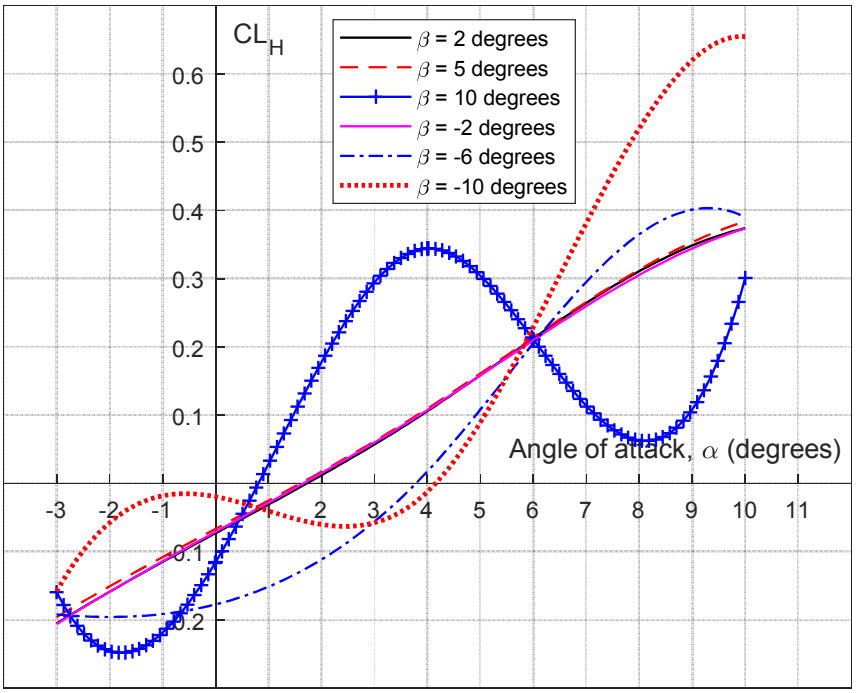

(b)

Figure 42: Horizontal tail lift coefficient vs angle of attack for different sideslip angles at 18 m/s and (a) 6500 RPM (b) 10000 RPM

To understand the dependency of the downwash angle ε_0 on the sideslip angle β, simulations carried out in Figure 42(a) were repeated for finer variations in the sideslip angle and is presented in Figure 43. From the figure, it is clear that ε_0 is a nonlinear function of the sideslip angle β. However, after a relatively low angle of attack of 4 degrees, the lift coefficient curves follow similar trends with very minimal variations in the lift coefficient values. There appears to be no valid explanation at this point for these strange anomalies. Hence, detailed study needs to be conducted in this regard to understand the nonlinear dependency of ε_0 on sideslip angle β and also the ineffectiveness of the horizontal tail at high sideslip angles as was observed in Figures 42 (a)-(b).

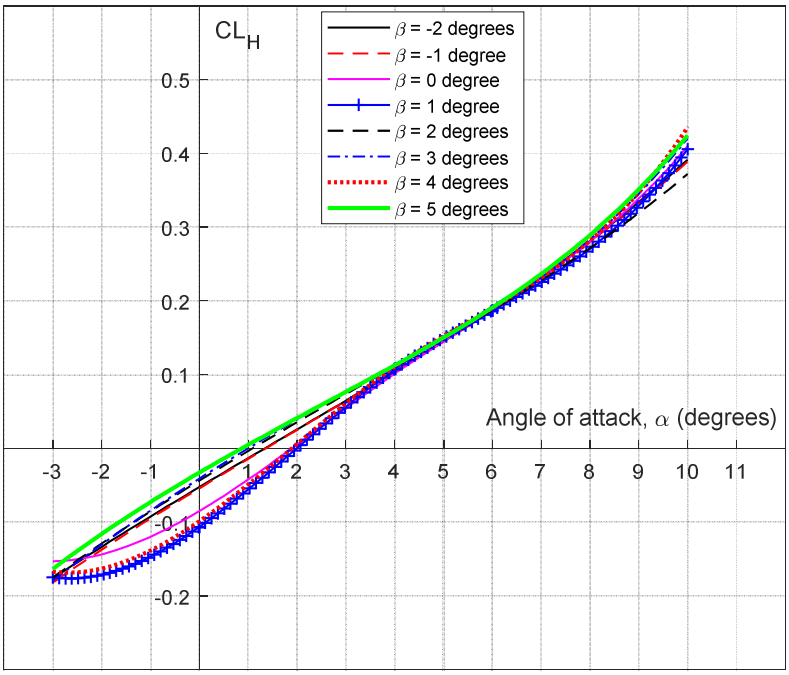

Figure 43: Horizontal tail lift coefficient vs angle of attack for finer sideslip angle variations at 18 m/s 6500 RPM

Finally, performance variations of the vertical tail were assessed for the simultaneous angle of attack and sideslip angle variations. Figure 44 indicates the side force coefficient generated by the vertical tail at different lateral-longitudinal attitudes of the aircraft and for a propeller rotation of 6500 RPM. It is clearly observed from Figure 44 that there seems to be a dependency of C_{YV} on angle of attack α which meant that the assumption in [6] again did not hold good for the DG808s. The side force coefficient is mostly linear if not completely, with the angle of attack for small to moderate changes in the sideslip angle. At high sideslip angles however, the side force coefficient appears to be a function of the angle of attack as observed from the curves for +10 and -10 degree sideslip angles.

The variation appears to be extremely nonlinear, leading to the assumption that the vertical tail is rendered ineffective at such high angles of attack. This is similar to the behavior that is seen in Figure 42(a-b) where the horizontal tail was completely ineffective at high sideslip angles. The nonlinear mixing of the different flow components due to the wing, vortices, slipstream and freestream air at the operating limit of the sideslip angle seems to reduce the performance of the vertical and horizontal tail sections almost completely.

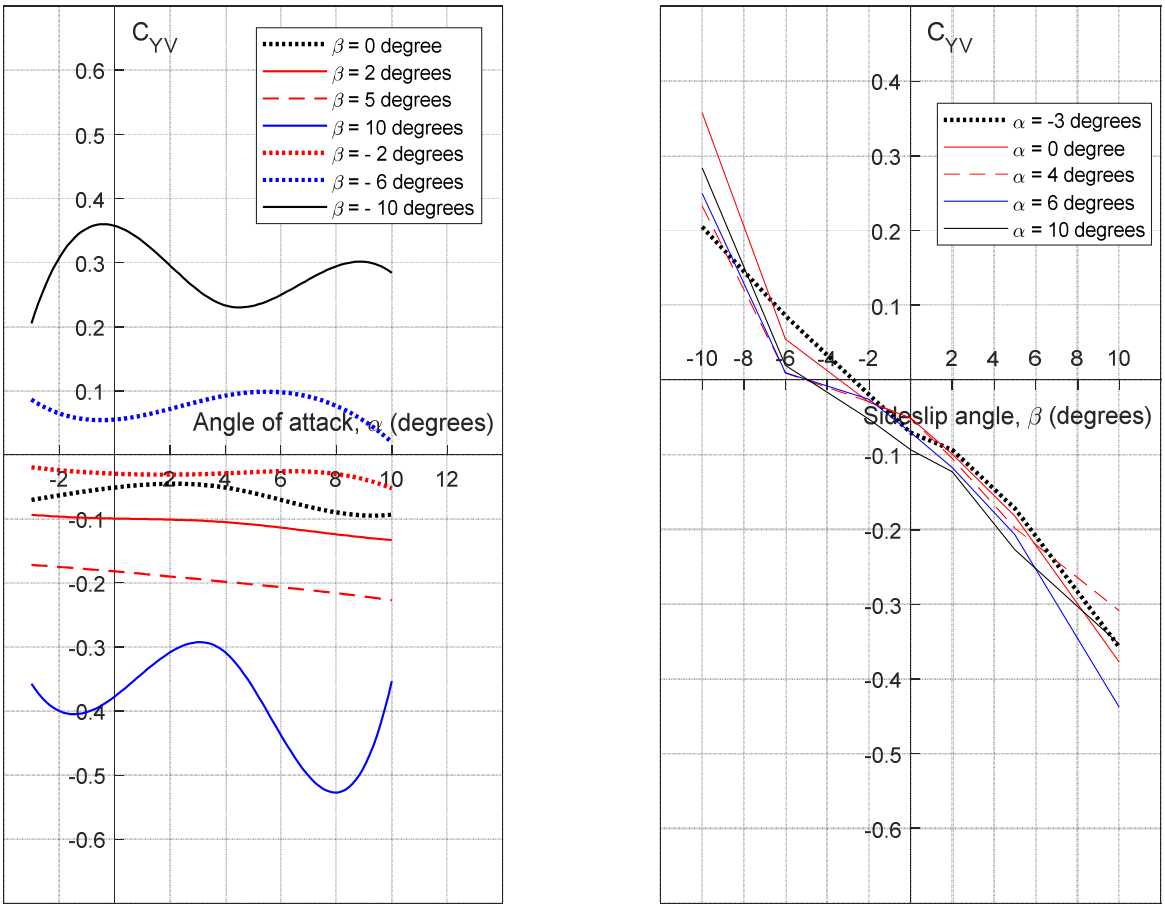

(a) (b)

Figure 44: Vertical tail side-force coefficient vs (a) angle of attack at different sideslip angles (b) sideslip angle at different angles of attack - 18 m/s and 6500 RPM - STAR-CCM+

Table 16 lists the maximum percentage difference in the zero sideslip sidewash angle (σ_0) as a variation of the angle of attack. The lowest value occurs at -3 degree angle of attack and the highest value is at 10 degree angle of attack. As observed from the table, the percentage discrepancy is large.

Table 16: Percentage difference in σ_0 due to angle of attack for 6500 RPM

Angle of attack (degrees)	Zero sideslip sidewash angle (σ_0) (degrees)	Maximum % difference
-3	-2.8	78.60%
10	-5	

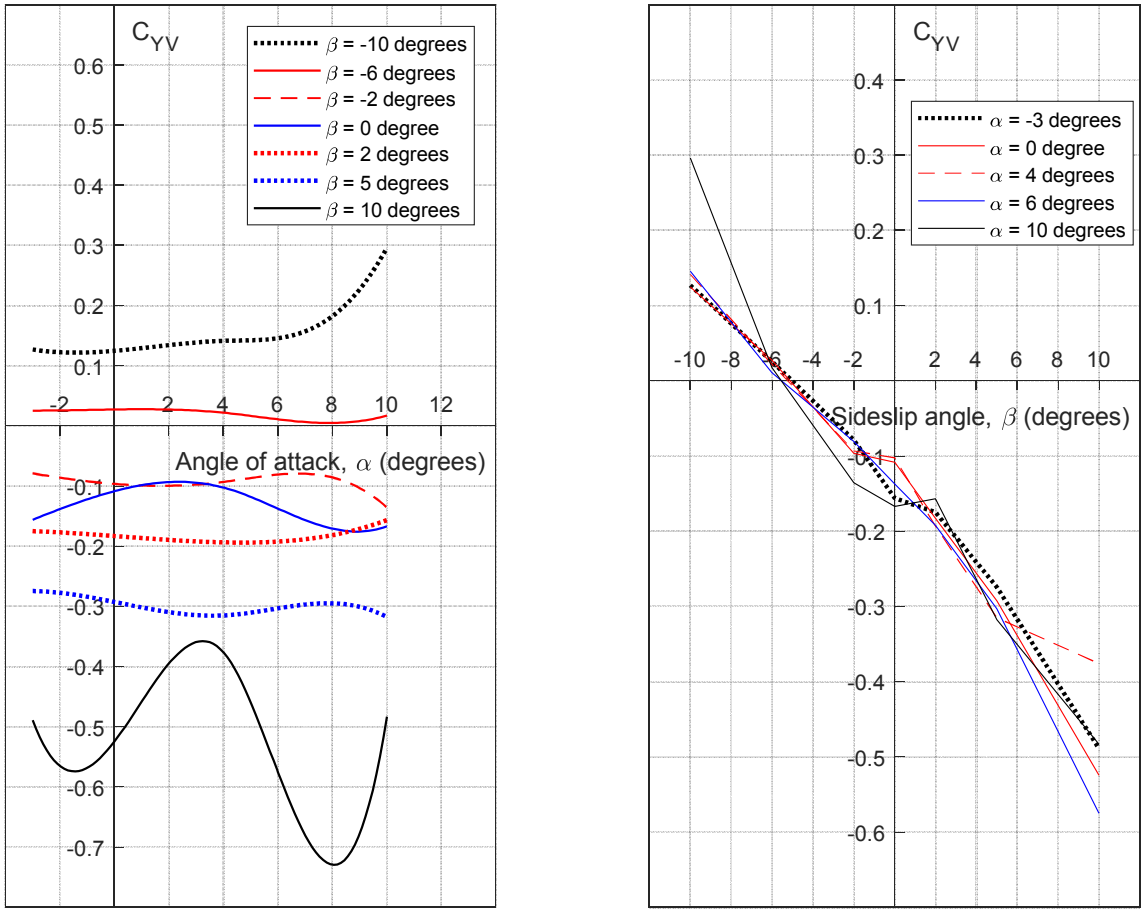

(a) (b)

Figure 45: Vertical tail side-force coefficient vs (a) angle of attack at different sideslip angles (b) sideslip angle at different angles of attack - 18 m/s and 10000 RPM - STAR-CCM+

The results presented in Figure 44 were repeated for 10,000 RPM and is presented in Figure 45. The curves seem to have attained a linear or semi-linear state due to the increase in propeller RPM. For the -10 degree sideslip angle, the curve appears to be quite linear with an abrupt increase close to stalling angle. This behavior is rather absurd and hard to explain. To provide conclusive

evidence and a valid explanation, a deeper study is required in this regard. An Interesting point to note however is that the impact of propeller RPM on zero sideslip sidewash angle (σ_0) is significant with an increase close to 100% than that for the 6500 RPM case.

Table 17: Percentage difference in σ_0 due to angle of attack for 10000 RPM

Angle of attack (degrees)	Zero sideslip sidewash angle (σ_0) (degrees)	Maximum % difference
-3	-5	14.00%
10	-5.7	

Based on Figure 45(b), the maximum percentage difference in the zero sideslip sidewash angle (σ_0) as a variation of the angle of attack for 10000 RPM was calculated and is listed in Table 17. Even though the percentage difference between the angles of attack reduced, the sidewash angle had a significantly larger value as compared to the 6500 RPM case.

Figures 46(a-b) further demonstrate the tail section behavior for simultaneous variations in airplane angle of attack and sideslip angles. As per the assumptions in [6], these gradients should have been zero and independent of each other which however is not the case from the data obtained. As observed from Figure 46(a), the variation of the horizontal tail downwash angle gradient with changes in sideslip angle are extremely large and nonlinear. This confirms some of the data obtained in Figure 42(a-b) wherein the horizontal tail became completely ineffective at high sideslip angles. Figure 46(b) indicates the variation in sidewash angles with changes in angle of attack. On the contrary to what has been obtained in Figure 46(a), the variation seems to be linear for the most part (up to 8 degree angle of attack) with nonlinearity occurring only at higher angles of attack close to stall. Although the curves point to the vertical tail being less affected by changes in angle of attack, it is hard to draw conclusions at this point. Most of the curves seem to follow a general trend but some curves behave out of proportion from the trends. Hence, it is necessary for detailed work to be done in this regard to establish a trend with the help of finer angle variations and more rotational speeds for the propeller.

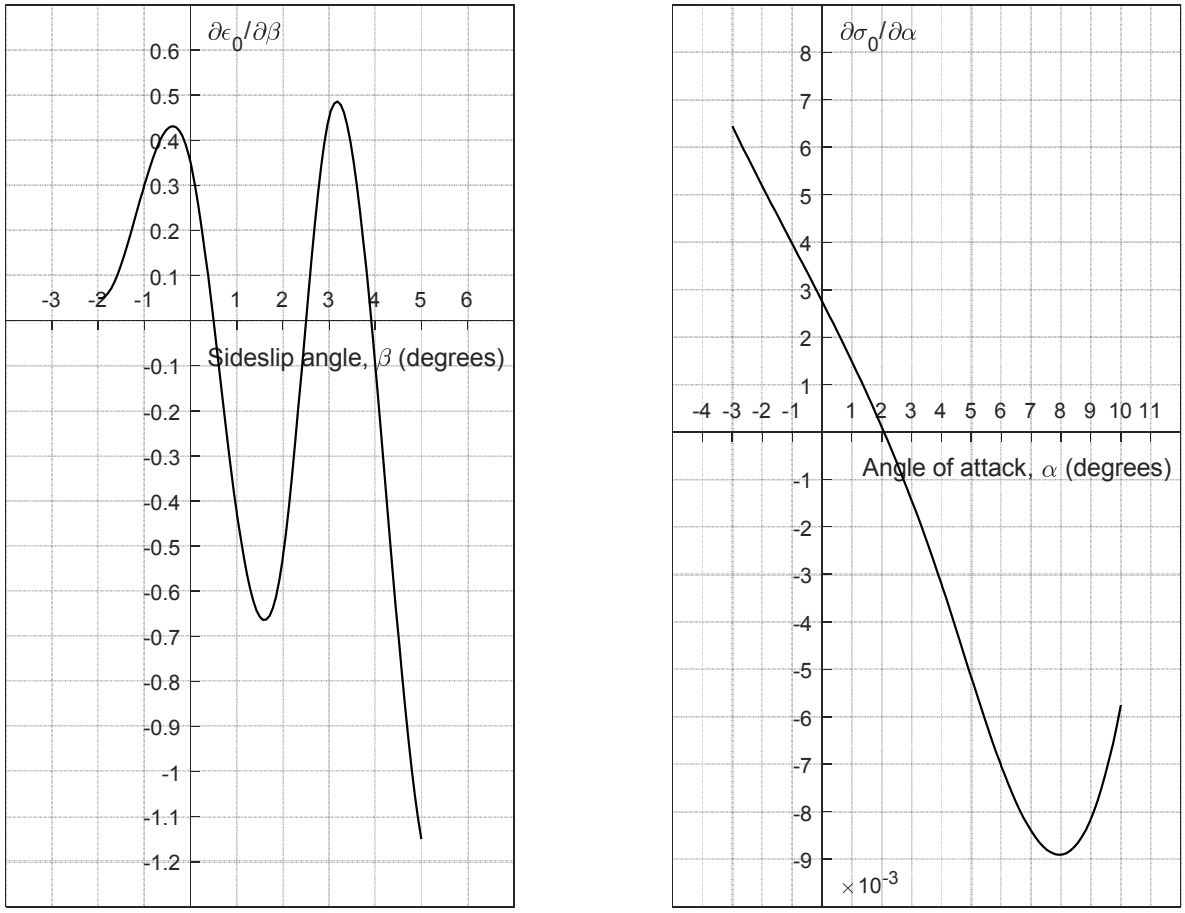

(a) (b)

Figure 46: Numerical gradients of (a) airplane zero angle of attack downwash angle with sideslip angle (b) airplane zero sideslip angle sidewash angle with angle of attack - 18m/s and 6500 RPM - STAR-CCM+

Chapter 7 . Conclusion

Aerodynamic performance data for the DG808s UAS in the propeller slipstream was successfully established with the aid of STAR-CCM+ which was then compared to data generated by the AAA software which is based on formulations and assumptions presented in [3] and [6]. A further comparison was also made with real time flight test data obtained through system identification to validate CFD results. Close comparison of data generated by both the softwares revealed discrepancies in the DG808s aerodynamic modeling between the two. Some of the major findings are concluded as follows.

- Longitudinal direction analysis:

  A large variation in ε_0 was observed on the horizontal tail due to the presence of the propeller wake which the AAA fell short in estimating. The findings of STAR-CCM+ confirmed work done in [18] - [20]. Phenomenon such as splitting up of the horizontal tail into two opposing sections of tangential velocities established in [18] and [20] were confirmed by the data generated through STAR-CCM+ in Figures 29 and 31. This strong component of the downward velocity was explained as the reason for the increase in downwash. A change in propeller RPM revealed that this downwash is further dependent on the magnitudes of the downward velocity components. A comparison of the airplane zero angle of attack lift coefficient with the real time flight test data was made with acceptable results. Discrepancies were accounted to the several factors not considered in the CFD models. The discrepancies between the data generated by STAR-CCM+ and AAA due to the propeller slipstream on the DG808s needs to be given thought and investigated further. The AAA data for longitudinal analysis however was in good agreement with that generated by STAR-CCM+ for the Poff configuration of the aircraft.
- Lateral direction analysis:

  Several interesting results were obtained again. To establish the authenticity of the CFD modeling, firstly a phenomenon stated in [5] was proved wherein the side-force generated by the vertical tail increased with the addition of different components of the aircraft. The side-force coefficient data was later compared with

the data generated by AAA and discrepancies were found again. AAA fell short in estimating performance data due to the propeller slipstream. For the Poff configuration, the side-force coefficients generated by STAR-CCM+ and AAA exhibit a linear and symmetric behavior as expected due to the symmetricity of the aircraft. When in the propeller slipstream however, an asymmetric and nonlinear behavior was observed. A comparison of the CFD data with system identification data from flight test confirmed these findings thus proving the reliability of estimations made by STAR-CCM+. Further, a direct relation was established between the sidewash angle, it's gradient, vertical tail C_{Y_V} and the propeller RPM/thrust. There were however certain aspects which lacked valid explanations and need to be looked at in detail (Figure 38).

- Simultaneous variations in longitudinal and lateral directions:

  To further understand the complexity of the flow in the slipstream, analysis for simultaneous variations in the longitudinal and lateral directions were carried out with significant findings again. The horizontal tail was rendered completely ineffective at high sideslip angles and in the slipstream. Similar findings were obtained for the vertical tail at high angles of attack as well. Changes in magnitudes of parameters also confirmed a direct dependency on propeller RPM. This meant that the decoupling assumption in [6] did not hold good for the DG808s in propeller slipstream. These findings however should be subject to further investigations.

All these findings appear to deviate from the assumptions made in [3], [6] and AAA which is based on correlating data for large aircraft wherein the aerodynamic centers of lifting surfaces are large distances apart. As mentioned earlier, UASs are relatively small aircraft with close proximity of lifting surfaces. In such cases, important flow phenomenon could vary nonlinearly based on geometrical configurations. In addition to the compactness, the propeller slipstream would have larger and significant effects due to its close proximity with the lifting surfaces. Hence, to model the aerodynamics and analyze the flight dynamics of UASs, influences due to the RPM and rotational configuration of the propeller if present and close proximity of components have to be factored in.

Having established comparisons with the AAA software however, the DG808s UAS has a very unconventional power plant configuration and complex geometry which is uncommon and specific to a small number of aircraft. In defense of the assumptions in [6] and AAA software, such UASs were nonexistent during development of the models and the software which may explain their underestimations in this case. The effectiveness of such software in the industry can be improved with frequent updates to the built-in aircraft model database. There also seems to be a need for a dedicated UAS design standard/procedure or modeling software with a wide database. To make completely autonomous aerial systems as explained in Section 1, higher fidelity methods such as CFD should be relied upon.

Chapter 8 . Recommendations and Future Scope of Work

To provide data for updates to engineering level software and to get a clearer perspective of the DG808s flight performance, the following recommendations are suggested.

- As discussed in Sections 6.1, 6.2, 6.3 and Chapter 7 of the report, a detailed study needs to be conducted in determining a valid explanation for the extremely nonlinear behavior of the $\frac{\partial C_{LH}}{\partial \alpha}$, $\frac{\partial C_{YV}}{\partial \beta}$, $\frac{\partial \epsilon_0}{\partial \beta}$ and $\frac{\partial \sigma_0}{\partial \alpha}$ curves in the propeller slipstream. Simulations and analysis for finer variations in the angles of attack and sideslip angles along with more rotational speeds for the propeller might provide more insight about these strange and unexplained behaviors. In addition to this, the behavior of the vertical tail for simultaneous variations in angle of attack and sideslip angle needs to be looked at in detail since some of the curves obtained in Section 6.3 exhibited strange characteristics hard to explain.
- Due to limited availability of computational resources and the time constraints, only steady state CFD simulations were analyzed. However, it will be interesting to see how the performance of the tail section varies with changes in time for which unsteady cases must be run. With this data, a more accurate comparison can also be made with flight tests. An important study will be the simultaneous variations in longitudinal and lateral direction w.r.t time. The performance variation due to change in angle of attack and sideslip angle for 0.1 second and 1 second for example may not be the same. This will provide more accurate data to aid the autonomy of the system in strong winds.
- For the current study, control surfaces on the aircraft were not modelled since baseline performance data had to be established. However, the propeller slipstream will have a considerable impact on the control surface effectiveness. Proof of this is available through flight tests, various textbooks and other published work. The effect of the propeller wake on the effectiveness of the rudder, elevator and the ailerons need to be studied.
- Since the DG808s electric glider has a T- Tail configuration, it is prone to deep stalling wherein the stalled air from the wing immerses the horizontal and vertical tail of the aircraft and renders them completely ineffective. Getting out of a deep stall is close to impossible due to the resulting highly unstable nature of the tail. A study can be carried out to observe the effects of the propeller on the aircraft at angles above and beyond stall.

Chapter 9 . References

[1] Smith, N.A., “Optimal Lateral Guidance for Automatic Landing of a Lightweight High Altitude Long Endurance Unmanned Aerial System with Crosswind Rejection”, The University of Kansas, Lawrence, Kansas, August 2016.

[2] Vivekanandan, P., Garcia, G., Yun, H., Keshmiri, S., “A Simplex Architecture for Intelligent and Safe Unmanned Aerial Vehicles”, IEEE 22nd International Conference on Embedded and Real-Time Computing Systems and Applications, 2011.

[3] Lan, E.C-T., Roskam, J., “Airplane Aerodynamics and Performance”, DARcorporation, Lawrence, Kansas, USA, 2001.

[4] Napolitano, M.R., “Aircraft Dynamics – From Modeling to Simulation”, John Wiley & Sons, Inc., 2012.

[5] Stengel, R.F., “Flight Dynamics”, Princeton university press, 2004.

[6] Roskam, J., “Airplane Flight Dynamics and Automatic Flight Controls”, Part I, DARcorporation, Lawrence, Kansas, USA, 2001.

[7] Hoak, D.E., et al., “The USAF Stability and Control DATCOM.”, Air Force Wright Aeronautical Laboratories, TR-83-2048, October 1960 (revised in 1978).

[8] Johnson, T.F., Tinoco, E.N., Yu, N.J., “Thirty Years of Development and Application of CFD at Boeing Commercial Airplanes, Seattle”, AIAA.

[9] Garcia, A.A., “CFD analysis of the SBXC glider airframe”, Naval Postgraduate School, Monterrey, California, June 2016.

[10] Hansen, T., “Modeling the Performance of the Standard Cirrus Glider using Navier-Stokes CFD”, Technical Soaring, Vol. 38, No. 1, January – March 2014.

[11] Bosman, J.J., “Refinement of Glider Aerodynamic Design using CFD”, Technical Soaring, Vol. 37, No. 2, April – June 2013.

[12] Theja, B.R., Dr. Gupta, M.S., “Design and Fluid Flow Analysis of Unmanned Aerial Vehicle (UAV)”, International Journal of Science and Research, Volume 4 Issue 11, November 2015.

[13] Hall, Z.M., “CFD Modeling of US Army UAVs using NASA's OVERFLOW CFD Code”, AIAA SciTech Forum, Grapevine, Texas, 9 – 13 January 2017.

[14] Lan, C.E., “An Analytical Investigation of Wing Jet Interaction”, Flight research laboratory, Department of Aerospace Engineering, The University of Kansas, April 1974.

[15] Jameson, A., “Analysis of Wing Slipstream Flow Interaction”, NASA CR-1632, 1970.

[16] Ribner H.S. and Ellis, N.D., “Theory and Computer Study of a Wing in a Slipstream”, AIAA Paper No. 66-466, 1966.

[17] Kleinstein, G. and Liu, C.H., “Application of Airfoil Theory for Nonuniform Streams to Wing Propeller Interaction”, Journal of Aircraft, Vol 9, No 2, February 1972.

[18] Chadha, S.A., Pomeroy, B.W. and Selig, M.S., “Computational Study of a Lifting Surface in Propeller Slipstreams”, AIAA Aviation, Washington, D.C., 13 – 17 June 2016.

[19] Fu, W., Li, J. and Wang, H., “Numerical Simulation of Propeller Slipstream Effect on A Propeller-driven Unmanned Aerial Vehicle”, International Conference on Advances in Computational Modeling and Simulation, 2011.

[20] Stuper, J., “Effect of Propeller Slipstream on Wing and Tail”, Technical Memorandums, National Advisory Committee for Aeronautics, Washington, August 1938.

[21] Ferrari, C., “Some Experiments of the Slipstream Effect”, Technical Memorandums, National Advisory Committee for Aeronautics, Washington, March 1937.

[22] Lan, C.E., “VORSTAB - A Computer Program for Calculating Lateral-Directional Stability Derivatives with Vortex Flow Effect”, NASA-CR-172501, January 1987.

[23] Cervinka, J., Kulhanek, R. and Patek, Z., “AN Airplane with Unconventionally Placed Propeller Power Units”, Acta Polytechnica 57(1): 1-7, 2017.

[24] Schroeijen, M.J.T., Veldhius, L.L.M. and Slingerland, R., "Propeller Slipstream investigation using the Fokker F27 Wind Tunnel Model with Flaps Deflected", 26th International Congress of the Aeronautical Sciences", 2008.

[25] "Effect of Propeller on Airplane Dynamics", [https://www.aircraftspruce.com/catalog/pdf/13-09032.pdf].

[26] Bouquet, T., Vos, R., "Modeling the Propeller Slipstream Effect on Lift and Pitching Moment", AIAA SciTech Forum, Grapevine, Texas, 9 – 13 January 2017.

[27] Strash, D.J., Lednicer, D.A., Rubin, T.D., "Analysis of Propeller Induced Aerodynamic Effects", AIAA, 1998.

[28] Kosik, A., "The CFD Simulation of The Flow Around the Aircraft using OPENFOAM and ANSA", 5th ANSA and μETA International Conference.

[29] Maqsood, A., Huei, F.H., Go, T.H., "Propeller-induced Effects on the Aerodynamics of a Small Unmanned Aerial Vehicle", J. Aerosp. Technol. Manag., Sao Jose dos Campos, Vol.4, pp. 475-480, Oct – Dec., 2012.

[30] Gamble, B.J. and Reeder, M.F., "Experimental Analysis of Propeller–Wing Interactions for a Micro Air Vehicle", Journal of Aircraft, Vol. 46, No. 1, January – February 2009.

[31] Yang, Q.E.G. and Li, F., "Numerical Analysis of the Interference Effect of Propeller Slipstream on Aircraft Flow Field", Journal of Aircraft, Vol. 35, No. 1, January – February 1998.

[32] Martin, C.A., "Power Effects on The Longitudinal Characteristics of Single-Engine Propeller-Driven Aircraft", Aerodynamics report, Department of Defence Support, Defence Science and Technology Organization Aeronautical Research Laboratories, Melbourne, Victoria, February 1983.

[33] Veldhuis, L.,"Propeller Wing Aerodynamic Interference" 28 June 2005.

[34] Schroijen, M.J.T., Dr. Slingerland, R., "Propeller slipstream effects on directional aircraft control with one engine inoperative", AIAA, 2007.

[35] Boudaoud, W., Yahiaoui, T., Imine, B. and Imine, O., “Effect of an External Vortex on The UAV Aerodynamic Performances”, EPJ Web of Conferences 25, 01104, 2012.

[36] Jonker, A.S., Bosman, J.J., Mathews, E.H. and Liebenberg, L., “Flow over a glider canopy”, The Aeronautical Journal, Volume 118 No. 1204, June 2014.

[37] Sharma, M., Reddy, T.R. and Ch. Priyadarsini, I., “Flow Analysis over an F-16 Aircraft using Computational Fluid Dynamics”, International Journal of Emerging Technology and Advanced Engineering, Volume 3, Issue 5, May 2013.

[38] Pepelea, D., Cojocaru, M.G., Toader, A., Niculescu, M.H., “CFD Analysis for UAV of Flying Wing”, Scientific Research and Education in the Air Force – AFASES 2016.

[39] Krasilnikov, V., Ponkratov, D. and Crepier, P., “A Numerical Study on the Characteristics of the System Propeller and Rudder at Low Speed Operation”, Second International Symposium on Marine Propulsors smp’11, Hamburg, Germany, June 2011.

[40] Selig, M.S., “Modeling Propeller Aerodynamics and Slipstream Effects on Small UAVs in Realtime”, AIAA Atmospheric Flight Mechanics Conference, Toronto, Ontario Canada, 2-5 August 2010.

[41] Hiemcke, C., “A Primer on Using CFD to Tackle UAV Aerodynamics Problems”, PhD, Fluent Inc.

[42] Silva, N.M.A., “Parametric Design, Aerodynamic Analysis and Parametric Optimization of a Solar UAV”, Tecnico Lisboa, June 2014.

[43] Katzoff, S., “Longitudinal Stability and Control with Special Reference to Slipstream Effects”, NACA report No. 690.

[44] Ribner, H.S., “Notes on the Propeller and Slipstream in Relation to Stability”, NACA Wartime Report, October 1944.

[45] Cebeci, T., Platzer, M., Chen, H., Chang, K.C. and Shao, J.P., “Analysis of Low-Speed Unsteady Airfoil Flows”, Springer, Horizons Publishing, 2005.

[46] Stone, R.H., “Aerodynamic Modeling of the Wing-Propeller Interaction for a Tail-Sitter Unmanned Air Vehicle”, Journal of Aircraft, Vol. 45, No. 1, January – February 2008.

[47] Phillips, W.F., “Estimating the Low-Speed Sidewash Gradient on a Vertical Stabilizer”, Journal of Aircraft, Vol. 39, No. 6, August 2002.

[48] Ortiz, A.D., Quiroz, L.E., Köck, R.A., “Aerodynamic Performance Analysis of a Low-Speed Acrobatic Airplane by Numerical Simulation”, First South-American Congress on Computational Mechanics, MECOM – 2002.

[49] Carpenter, C., “Splitting domains for rotation”, Steve Portal, CD-ADAPCO.

[50] Drela, M., “XFOIL”, Massachusetts Institute of Technology.

[51] Anderson, J.D., “Fundamentals of Aerodynamics”, McGraw-Hill Education, 5th edition, February 2010.

[52] https://people.rit.edu/pnveme/personal/EMEM682n/StaticStab/direction_control.html

[53] https://pt.wikipedia.org/wiki/%C3%82ngulo_de_derrapagem_(aeron%C3%A1utica)